2009

First passage time analysis for climate prediction

Chu, Peter C.

Chu, P.C., 2009: First passage time analysis for climate prediction. In: Stochastic Physics and Climate Modelling, edited by T. N. Palmer and P. Williams, Chapter 6, Cambridge University Press (ISBN-13:9780521761055), 157-190

http://hdl.handle.net/10945/36318

P1: SJT Trim: 174mm × 247mm Top: 0.553in Gutter: 0.747in
CUUK726-06 cuuk726/Palmer ISBN: 978 0 521 76105 5 July 6, 2009 17:42

6

First passage time analysis for climate prediction

PETER C. CHU

Climate prediction experiences various input uncertainties such as initial condition errors (predictability of the first kind), boundary condition (or model parameter) errors (predictability of the second kind), and combined errors (predictability of the third kind). Quantification of model predictability due to input uncertainties is a key issue leading to successful climate prediction. The first passage time (FPT), defined as the time period when the prediction error first exceeds a predetermined criterion (i.e. the tolerance level) can be used to quantify the model predictability. A theoretical framework on the basis of the backward Fokker–Planck equation is developed to determine the probability distribution function of FPT. Furthermore, the FPT analysis can also be used for climate index prediction.

6.1 Introduction

Complexity in climate systems makes prediction difficult. Numerical modelling and climate index prediction are often used. For numerical climate modelling, a practical question is commonly asked: How long is a climate model valid since being integrated from its initial state? To answer this question, the instantaneous error (IE, defined as the difference between the prediction and reality), must be investigated. It is widely recognised that the IE is caused by the three types of model uncertainties (Lorenz 1984): (a) measurement errors, (b) model errors such as discretisation and uncertain model parameters, and (c) chaotic dynamics. Measurement errors cause uncertainty in initial and/or boundary conditions. Such a method using the IE evolution with respect to uncertain model input is called the forward approach.

For the forward approach, the small amplitude stability analysis (linear error dynamics) is used with the IE growth rate and the corresponding e-folding time scale as the measures for evaluating the model predictability due to initial condition error

P1: SJT Trim: 174mm × 247mm Top: 0.553in Gutter: 0.747in
CUUK726-06 cuuk726/Palmer ISBN: 978 0 521 76105 5 July 6, 2009 17:42

(the first kind of predictability). The IE growth rate is usually estimated by either the leading (largest) Lyapunov exponent or the amplification factors calculated from the leading singular vectors (SVs) (Dalcher and Kalnay 1987). However, the errors may grow to finite amplitudes such as in medium-range prediction (Vukicevic 1991), in forecasting using 'imperfect' models (Bofetta *et al*. 1998) and in models with open boundaries (Chu 1999). The linear assumption is no longer applicable and the nonlinear effect should be considered.

One way to simplify the climate system is to represent low-frequency variability of atmospheric circulations by climate indices, i.e. teleconnection patterns, such as the Arctic Oscillation (AO), Antarctic Oscillation (AAO), North Atlantic Oscillation (NAO), Pacific/North American Pattern (PNA) and Southern Oscillation (SO). Temporally varying indices, $s(t)$, were calculated for these patterns. Here, t denotes time. Among them, the SO index (SOI) was first to show equivalent barotropic seasaw in atmospheric pressure between the southeastern tropical Pacific and the Australian–Indonesian regions (Walker and Bliss 1937). A popular formula for calculating the monthly SOI is proposed by the Australian Bureau of Meteorology,

$$s(t) = 10 \times \frac{p_{\text{diff}}(t) - \langle p_{\text{diff}} \rangle}{SD(p_{\text{diff}})}. \tag{6.1}$$

Here, p_{diff} is the mean sea-level pressure of Tahiti minus that of Dawin for that month; $\langle p_{\text{diff}} \rangle$ is the long-term average of p_{diff} for the month in question; and $SD(p_{\text{diff}})$ is the long-term standard deviation of p_{diff} for the month in question. Detailed information can be found at http://www.cpc.noaa.gov/.

How to predict the climate indices effectively has practical significance because of their connections to large-scale atmospheric circulation. Usually, these indices are treated as time series and statistical predictions are conducted (forward method). For example, singular spectrum analysis (Keppenne and Ghil 1992), wavelet analysis (Torrence and Campo 1998), and nonlinear analogue analysis (Drosdowsky 1994) were used to obtain the dominant frequencies of the SOI time series. The power-law correlations were found for the self-affine properties of SOI (Ausloos and Ivanova 2001). Such methods may be called the forward index prediction.

An alternative 'backward' method may be used for numerical climate modelling, index prediction and model predictability detection. This method predicts a typical time span (τ) needed for the IE to first exceed a pre-determined criterion (i.e. the tolerance level) in numerical modelling or for a climate index to exceed a given increment. Such a time span (τ) is defined as the first passage time (FPT), which is widely used in many disciplines such as nonlinear dynamical systems (e.g. Ivanov *et al*. 1994), physics and chemistry (e.g. Rangarajan and Ding 2000), biology and economics (e.g. Chu 2006), etc., but not in meteorology and climatology until recently when the FPT was used to evaluate ocean–atmospheric

P1: SJT Trim: 174mm × 247mm Top: 0.553in Gutter: 0.747in
CUUK726-06 cuuk726/Palmer ISBN: 978 0 521 76105 5 July 6, 2009 17:42

model predictability (Chu *et al*. 2002a,b,c) and to predict the climate indices (Chu 2008). In this chapter, we will introduce the FPT concept and its broad application in climate studies. The rest of the paper is outlined as follows. Sections 5.6.2 and 6.3 discuss the forward and backward approaches. Sections 5.6.4 and 6.5 describe the backward Fokker–Planck equation (for FPT) and the moments of FPT. Section 6.6 presents the stochastic stability and Section 6.7 shows the power decay law of FPT and its moments. Section 6.8 depicts identification of the Lagrangian stability using FPT analysis and Section 6.9 presents the conclusions.

6.2 Forward approach

The forward approach is commonly used in climate studies. Here, two examples are listed for comparison to the backward approach.

6.2.1 Climate index prediction

Monthly varying climate indices from the National Oceanic and Atmospheric Administration (NOAA) Climate Prediction Center show randomness (Fig. 6.1) with poor predictability because their phases and amplitudes are rather unpredictable; both involve many (time and space) scales which are often intrinsic to chaotic behavior. The forward approach predicts the change of the index (z) at time t with a given temporal increment τ from analysing single or multiple time series. Due to the stochastic nature, the probability density function (PDF), $p[z(t), \tau]$, should first be constructed. Collette and Ausloos (2004) analysed the NAO monthly index (single time series) from 1825 till 2002 and found that the long-range time correlations are similar to Brownian fluctuations.

The distribution functions of the NAO monthly index fluctuations have a form close to a Gaussian, for all time lags. This indicates the lack of predictive power of the present NAO monthly index. Lind *et al*. (2005) used the standard Markov analysis to get the Chapman–Kolmogorov equation for the conditional PDF of the increments z of the NAO index over different time intervals τ and to compute the diffusion and drift coefficients ($D^{(1)}$, $D^{(2)}$) from the first two moments of such a probability distribution. The random variable $z(t)$ is found to satisfy the Langevin equation

$$\frac{\mathrm{d}z(t)}{\mathrm{d}t} = D^{(1)}[z(t), t] + \eta(t)\sqrt{D^{(2)}[z(t), t]} \tag{6.2}$$

where $\eta(t)$ is a fluctuating δ-correlated force with Gaussian statistics, i.e.

$$\langle \eta(t) \rangle = 0, \ \langle \eta(t)\eta(t') \rangle = q^2 \delta(t - t'). \tag{6.3}$$

P1: SJT Trim: 174mm × 247mm Top: 0.553in Gutter: 0.747in
CUUK726-06 cuuk726/Palmer ISBN: 978 0 521 76105 5 July 6, 2009 17:42

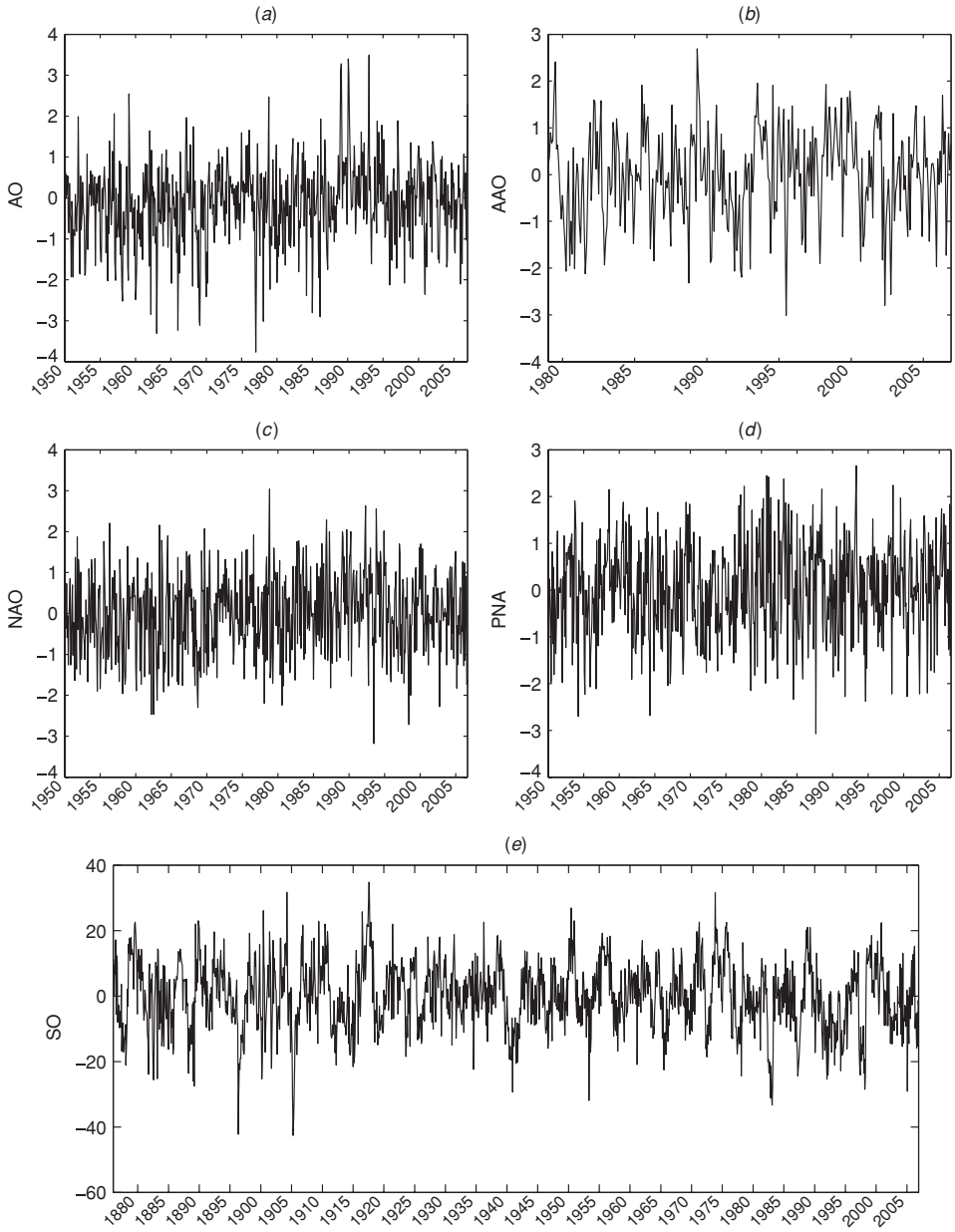

Figure 6.1 The monthly mean climate index data obtained from NOAA Climate Prediction Center for: (*a*) Arctic Oscillation (AO), (*b*) Antarctic Oscillation (AAO), (*c*) North Atlantic Oscillation (NAO), (*d*) Pacific/North American Pattern (PNA), and (*e*) Southern Oscillation (SO). Detailed information can be found at http://www.cpc.noaa.gov/.

P1: SJT Trim: 174mm × 247mm Top: 0.553in Gutter: 0.747in
CUUK726-06 cuuk726/Palmer ISBN: 978 0 521 76105 5 July 6, 2009 17:42

Maharaj and Wheeler (2005) predict the daily bi-variate index (multiple time series) of the Madden–Julian oscillation using seasonally varying vector autoregressive models. Although this model shows no strong skill advantage over a lagged regression technique, it has the convenience of employing only a single set of equations to make predictions for multiple forecast horizons.

6.2.2 Model predictability

Let climate evolution in domain Ω be described by the dynamical state vector $\mathbf{X}(\mathbf{x}, t)$ determined to be composed from variables such as pressure, velocity, temperature, humidity, salinity and so on with $(\mathbf{x}, t)$ denoting the spatial and temporal coordinates. In general this vector may only be approximately estimated from the observations. In order to overcome this complexity the estimation of model forecast skill is reduced into the sensitivity analysis of the so-called 'reference solution' $\mathbf{X}_{\text{ref}}$ $(\mathbf{x}, t)$ to perturbations of model input (Lacarra and Talagrand 1988). The numerical climate model is usually represented by

$$\mathrm{d}\mathbf{Y}/\mathrm{d}t = \mathbf{F}(\mathbf{Y}, t), \tag{6.4}$$

with the initial condition

$$\mathbf{Y}(\mathbf{x}, t_0) = \mathbf{Y}_0, \tag{6.5}$$

and the boundary conditions

$$\mathbf{G}(\mathbf{Y}(\mathbf{x}, t)) = \mathbf{Q}, \tag{6.6}$$

where $\mathbf{F}(\mathbf{Y}, t)$ is a nonlinear operator describing forcing, nonlinear interactions and subgrid parameterisations, $\mathbf{Y}_0$ is the initial vector and $\mathbf{G}$ determines fluxes across the boundary of calculation domain Ω. When the IE is defined by

$$\mathbf{Z}(\mathbf{x}, t) = \mathbf{Y}(\mathbf{x}, t) - \mathbf{X}_{\text{ref}}(\mathbf{x}, t), \mathbf{Z}(\mathbf{x}, t_0) = \mathbf{Z}_0,$$

the model predictability is estimated by a dimensionless functional

$$J(\mathbf{Z}, \mathbf{W}, t) = \left\{\mathbf{Z}^{\mathrm{T}}\mathbf{W}\mathbf{Z}\right\}, \tag{6.7}$$

where $\mathbf{W}(\mathbf{x}, t)$ is the weight matrix, the superscript 'T' denotes the transpose operator, and the brackets denote the volume integration $\{\ldots\} = \iiint_{\Omega} \ldots \mathrm{d}V$.

From the physical point of view, the functional J satisfies the two following inequalities,

$$\langle J(\mathbf{Z}, \mathbf{W}, t)\rangle \geq J_{\text{noise}} = \left\langle\left\{\mathbf{Z}^{\mathrm{T}}_{\text{noise}}\mathbf{Z}_{\text{noise}}\right\}\right\rangle,$$
$$\langle J(\mathbf{Z}, \mathbf{W}, t)\rangle \leq \varepsilon_0 \left\{\mathbf{X}^{\mathrm{T}}_{\text{ref}}\mathbf{X}_{\text{ref}}\right\},$$

P1: SJT Trim: 174mm × 247mm Top: 0.553in Gutter: 0.747in
CUUK726-06 cuuk726/Palmer ISBN: 978 0 521 76105 5 July 6, 2009 17:42

where the angular brackets show the ensemble averaging; $\mathbf{Z}_{\text{noise}}$ characterises the level of non-removed noise existing in the model such as the natural heating noise. In general the level of the intrinsic model noise is determined by the chosen parameterisation schemes for unresolved scales (Chu *et al*. 2002b); and $\varepsilon = \varepsilon_0\{\mathbf{X}_{\text{ref}}^{\text{T}}\mathbf{X}_{\text{ref}}\}$ is the allowed model uncertainty (tolerance level) for the prediction.

The forward approach is to find the temporal evolution of the functional $J(\mathbf{Z}, \mathbf{W}, t)$. The model evaluation becomes a stability analysis on small-amplitude errors in terms of either the leading (largest) Lyapunov exponent or can be calculated from the leading singular vectors (Farrell & Ioannou 1996). The faster the IE grows, the shorter the e-folding scale is. For finite-amplitude IE, however, the linear stability analysis becomes invalid. The statistical analysis of the instantaneous error (both small- and finite-amplitudes) growth (Nicolis 1992), the information–theoretical principles for the predictability power (Schneider and Griffies 1999) and the ensembles for forecast skill identification (Toth *et al*. 2001) become useful. Such methods may be called the forward model predictability.

The linear tangent model of the IE dynamics is commonly used to estimate the prediction time scale through leading (largest) Lyapunov exponents or the amplification factors calculated from the leading singular vectors (the finite-time Lyapunov exponents). Linearisation of the governing equations is realistic when the energy of IE is considerably less than the energy of the reference solution (Palmer 2001). With the linear tangent model, the energy is transferred from the (basic) flow to the perturbations (error field), not vice versa. However, many studies show the existence of upscale processes when the energy is transferred the small scale to large scale perturbations. In this case the nonlinear IE dynamics should be considered even if formally the energy of the reference solution dominates. Thus, approaches that automatically incorporate both linear and nonlinear perspectives of IE should be considered in ocean models especially in regional and coastal oceans.

Both linear and nonlinear perspectives of IE and corresponding prediction timescales are computed through the probabilistic approach based on the PDF of IE. In general, such a PDF satisfies the Liouville or Fokker–Planck equation (Nicolis 1992). In practice, because the dimension of error subspace is high for large models, the low-order moments of PDF, such as mean and variance, can be estimated only through ensemble averaging techniques (Toth & Kalnay 1997), i.e. practically the error distribution is assumed to be approximately Gaussian. That simplifies mathematics but often does not agree with the physics of circulation in small semi-closed seas. Using the Gulf of Lion as an example, Auclair *et al*. (2003) pointed out that in coastal ocean modeling, the IE statistics remain largely unknown (they are probably not even exactly Gaussian) and such a well-behaved homogeneous (or even regionally homogeneous) statistical description could seem rather over-simplistic.

P1: SJT Trim: 174mm × 247mm Top: 0.553in Gutter: 0.747in
CUUK726-06 cuuk726/Palmer ISBN: 978 0 521 76105 5 July 6, 2009 17:42

6.3 Backward approach and FPT

6.3.1 Climate index prediction

The climate indices change either positively or negatively at a given time (Fig. 6.1). Then, of course, it is of interest to predict the exact change at a point in time; however, this is not possible. Therefore, the best one can do, from a statistical point of view, is to predict the time that is probabilistically favourable for the given index change. This optimal time, as we will see, is determined by the maximum of the first passage time distribution, i.e. the optimal FPT. Given a fixed value of an index reduction (z), the corresponding time span (positive) is estimated for which the index reduction (similar for index enhancement)

$$\gamma_{\Delta t}(t) = s(t + \Delta t) - s(t), \tag{6.8}$$

reaches the level ρ for the first time (Chu 2008),

$$\tau_\rho(t) = \inf\{\Delta t > 0 | \gamma_{\Delta t}(t) \leq -\rho\}, \tag{6.9}$$

which is a random variable and called the FPT. As the index data run through the past history, the FPT can be computed and the PDF of FPT, $p(\tau_\rho)$, can be constructed. Fig. 6.2 shows $p(\tau_\rho)$ with $\rho = 1.9$ for AO, AAO, NAO, PNA indices and with $\rho = 25$ for SOI. The solid curve is the theoretical PDF, which will be discussed in Section 6.4.

The PDF of FPT exhibits a rather well defined and pronounced maximum, followed by an extended tail for very long FPTs indicating a non-zero and important probability of large passage times (note that the τ_ρ-axis is logarithmic). These long (toward El Niño for SOI) FPTs reflect periods where the tropical Pacific is in a strong El Niño phase and needs a long period of time before finally coming to an even stronger El Niño. The short FPTs on the other hand – those around the maximum – are in La Niña periods, which appear to be the most common scenario. A cumulative distribution is introduced for transition times larger than τ_ρ, i.e.

$$P(\tau_\rho) = \int_{\tau_\rho}^{\infty} p(\tau) \mathrm{d}\tau. \tag{6.10}$$

To better understand the tail of this distribution, various values of ρ are considered. If this level is small enough, it is likely that the index reduction will break through the level after the first month, while larger FPTs will become more and more unlikely. However, the probability for a large FPT value will not be zero; if, say, there is a small-level ρ, then a period of strong El Niño will result in a $\tau_\rho(t)$ that might be considerably larger than one month since it takes time to recover from the El Niño event. For instance, after the 1992 El Niño event, it took five years to reach a new El Niño event in 1997.

P1: SJT Trim: 174mm × 247mm Top: 0.553in Gutter: 0.747in
CUUK726-06 cuuk726/Palmer ISBN: 978 0 521 76105 5 July 6, 2009 17:42

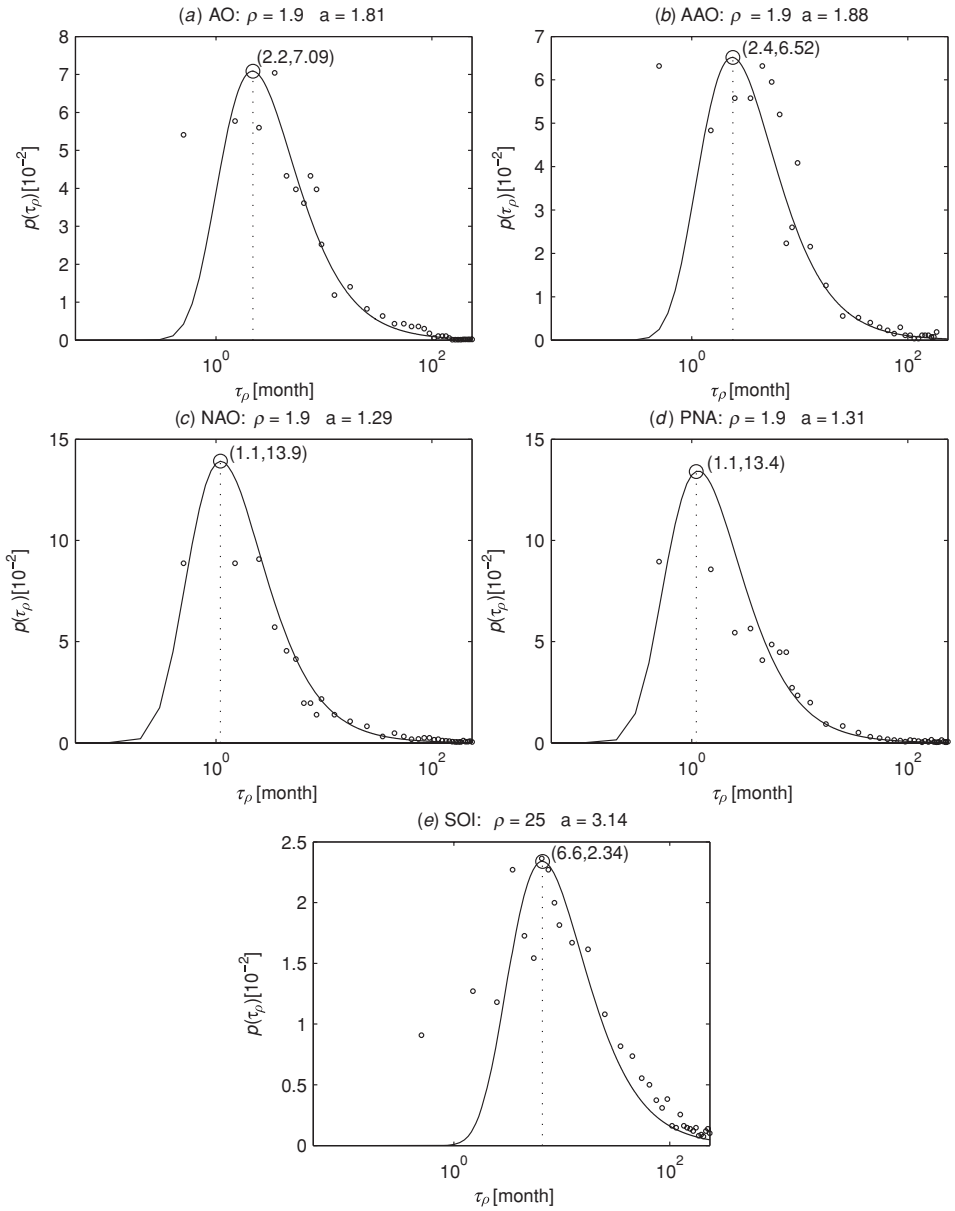

Figure 6.2 First passage time density functions with particular index reduction ρ for (*a*) Arctic Oscillation (AO), (*b*) Antarctic Oscillation (AAO), (*c*) North Atlantic Oscillation (NAO), (*d*) Pacific/North American Pattern (PNA) and (*e*) Southern Oscillation (SO) (after Chu 2008). Here, the parameter a represents the most favourable FPT, $\tau_\rho^{(\max)} = 2a^2/3$, which is the first value in parenthesis near the curve maxima. The second value is its PDF.

P1: SJT Trim: 174mm × 247mm Top: 0.553in Gutter: 0.747in
CUUK726-06 cuuk726/Palmer ISBN: 978 0 521 76105 5 July 6, 2009 17:42

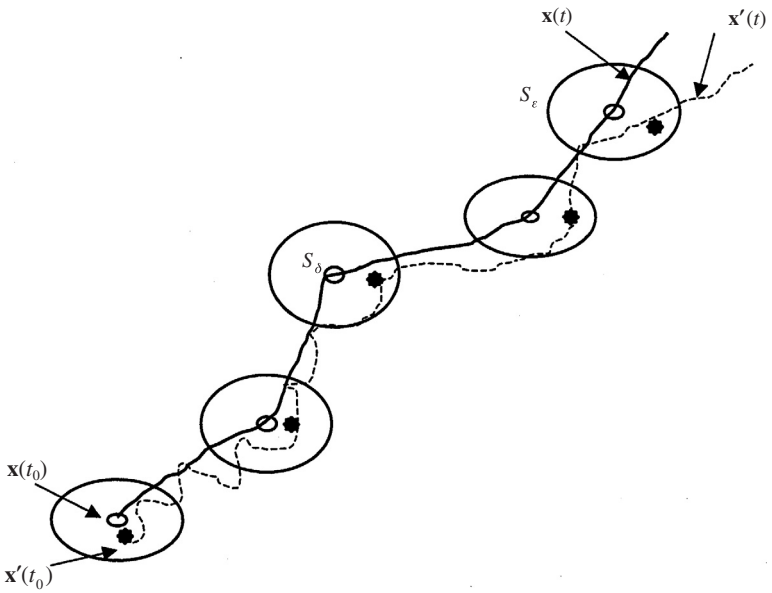

Figure 6.3 Trajectories of model prediction **y** (solid curve) and reality **x** (dashed curve) and error ellipsoid $S_\varepsilon(t)$ centered at y. The reality and prediction trajectories at a time instance are denoted by '*' and 'o ', respectively). A valid prediction is represented by a time period $(t - t_0)$ at which the error first goes out of the ellipsoid $S_\varepsilon(t)$ (after Chu *et al*. 2002b).

6.3.2 Model predictability

The backward approach is to find a time period τ (i.e. FPT) at which the functional $J(\mathbf{Z}_0, \mathbf{W}, t)$ reaches a predetermined tolerance level (ε) for the first time,

$$\tau\,(\mathbf{Z}_0, \mathbf{W}, \varepsilon) = \inf_{t\geq 0}(t \,|\, J(\mathbf{Z}_0, \mathbf{W}, t) > \varepsilon^2). \tag{6.11}$$

The prediction is valid if the state point $\mathbf{x}(t)$ is situated inside the ellipsoid (S_ε, called tolerance ellipsoid) with center at $\mathbf{y}(t)$ (i.e. the prediction) and size ε. When $\mathbf{y}(t)$ coincides with $\mathbf{x}(t)$, the model has perfect prediction. The prediction is invalid if the state point $\mathbf{x}(t)$ first touches the boundary of the tolerance ellipsoid the FPT for prediction is the time period from the initial state (Fig. 6.3).

The FPT is a random variable when the model has stochastic forcing or the initial condition has a random error. Its statistics such as the probability density function, mean and variance can represent how long the model can predict. For simplicity and without loss of generality, a one-dimensional population model is used for illustration. Clearly, the FPT defines the model predictability on the condition that any returns of model predictability (i.e. model error smaller than the tolerance level ε after passing the FPT) do not contribute to the prediction skill (the shaded zones

P1: SJT Trim: 174mm × 247mm Top: 0.553in Gutter: 0.747in
CUUK726-06 cuuk726/Palmer ISBN: 978 0 521 76105 5 July 6, 2009 17:42

in Fig. 6.4*a*). The mean FPT differs from the e-folding or the doubling time when J oscillates or is random. To compare the e-folding and the FPT, we need to assume in (6.11) that

$$J_{\text{norm}} = (\mathbf{Z}_0, \mathbf{Z}_0) \text{ and } \hat{\varepsilon}^2 = e^2.$$

The e-folding time is the time when $\langle J \rangle$ crosses e^2 (Fig. 6.4*b*),

$$\tau_{\text{e}}(\mathbf{W}) = \max_{t \geq 0}(t | \langle J(\mathbf{Z}_0, \mathbf{W}, t) \rangle \leq e^2), \tag{6.12}$$

where the brackets denote the average over the ensemble of initial perturbations $\mathbf{Z}_0$. The mean FPT for the same e is computed by

$$\langle \tau(\mathbf{W}, e) \rangle = \langle \inf_{t \geq 0}(t | J(\mathbf{Z}_0, \mathbf{W}, t) > e^2) \rangle, \tag{6.13}$$

where the averaging is over the ensemble of FPTs $(\tau_1, \ldots, \tau_N)$ induced by the ensemble of $\mathbf{Z}_0$ (Fig. 6.4*c*). Chu and Ivanov (2005) pointed out that the mean FPT is the lower bound of e-folding time:

$$\tau_{\text{e}}(\mathbf{W}) \geq \langle \tau(\mathbf{W}, e) \rangle.$$

6.4 Backward Fokker–Planck equation

Despite the linearity or nonlinearity of the original dynamical system, the PDF of FPT always satisfies a linear equation called the backward Fokker–Planck equation. For a random variable z satisfying the Langevin equation (6.2), the corresponding backward Fokker–Planck equation (Gardiner 1985; Chu *et al*. 2002a; Chu 2008) is given by

$$\frac{\partial p}{\partial t} - [D^{(1)}(z, t)]\frac{\partial p}{\partial z} - \frac{1}{2}\eta^{(2)} D^{(2)}(z, t)\frac{\partial^2 p}{\partial z^2} = 0, \tag{6.14}$$

which has an analytical solution,

$$p(\tau) = \frac{1}{\sqrt{\pi}}\frac{a}{\tau^{3/2}} \exp\left(-\frac{a^2}{\tau}\right), a > 0, \tau > 0. \tag{6.15}$$

The Lorenz system (1984) is the simplest possible model capable of representing an unmodified or modified Hadley circulation, determining its stability, and, if it is unstable, representing a stationary or migratory disturbance. Projection of the three-dimensional forecast error vector onto the unstable manifold leads to a self-consistent model (Nicolis 1992)

$$\frac{\mathrm{d}\xi}{\mathrm{d}t} = (\sigma - g\xi)\xi + \eta(t)\xi, \xi|_{\text{t=t}_0} = \xi_0, \xi \in (0, \infty), \tag{6.16}$$

P1: SJT Trim: 174mm × 247mm Top: 0.553in Gutter: 0.747in
CUUK726-06 cuuk726/Palmer ISBN: 978 0 521 76105 5 July 6, 2009 17:42

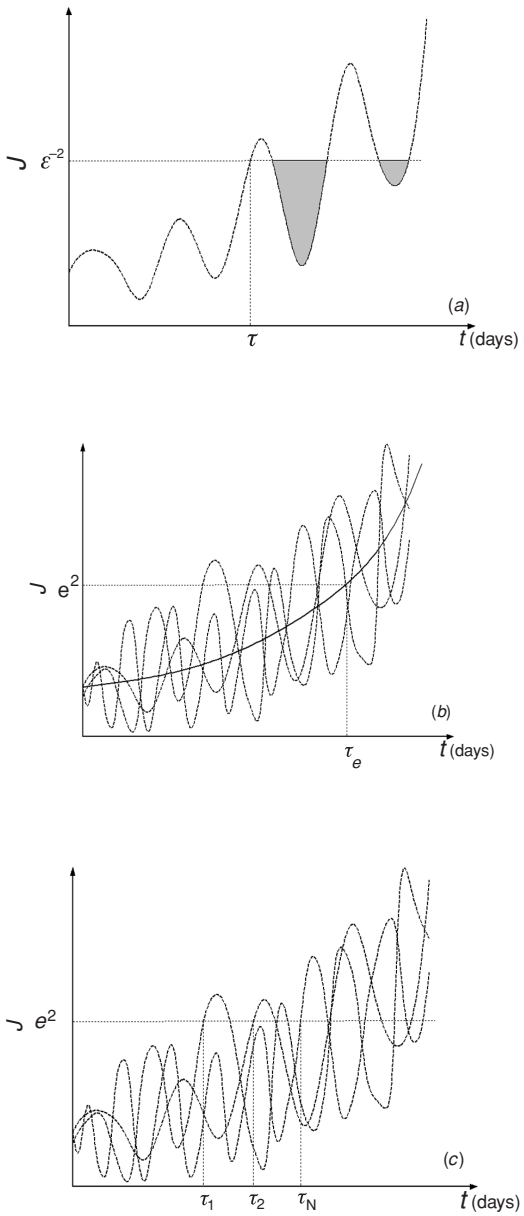

Figure 6.4 The FPT and e-folding time for an oscillating prediction error: (*a*) FPT (τ) computed in an individual forecast (shaded zones show returns of model predictability), (*b*) an ensemble of J (dashed curves), the ensemble averaged J (solid curve) and the e-folding time (τ_e); and (*c*) the ensemble of J (dashed curves) and appropriate ensemble of FPT ($\tau_1, \tau_2, \ldots, \tau_N$) (after Ivanov and Chu 2007a,b).

P1: SJT Trim: 174mm × 247mm Top: 0.553in Gutter: 0.747in
CUUK726-06 cuuk726/Palmer ISBN: 978 0 521 76105 5 July 6, 2009 17:42

where ξ is non-dimensional amplitude of error, g is a non-negative, generally time-independent nonlinear parameter whose properties depend on the underlying attractor; and $\eta(t)$ is a fluctuating δ-correlated force with Gaussian statistics [see (6.3)]. The PDF of FPT satisfies the following backward Fokker–Planck equation (Chu *et al*. 2002a,b),

$$\frac{\partial p}{\partial t} - \left(\sigma\xi_0 - g\xi_0^2\right)\frac{\partial p}{\partial \xi^0} - \frac{1}{2}q^2\frac{\partial^2 p}{\partial \xi_0^2} = 0, \tag{6.17}$$

with the initial error (ξ_0) bounded by,

$$\xi_{\text{noise}} \le \xi_0 \le \varepsilon. \tag{6.18}$$

6.5 Moments of FPT

With the known PDF of FPT, the k-th moment and central moment ($k = 1, 2, \dots$) of FPT is calculated by

$$\tau_k = k\int_0^\infty p(\tau)(\tau)^{k-1}\mathrm{d}\tau, \quad \hat{\tau}_k = k\int_0^\infty p(\tau)(\tau-\tau_1)^{k-1}\mathrm{d}\tau \quad k = 2, \dots, \infty, \tag{6.19}$$

where τ_1 and $\hat{\tau}_2$ are the mean and variance of the FPT, and

$$\mathrm{SK} \equiv \hat{\tau}_3/\hat{\tau}_2^{3/2}, \mathrm{KU} \equiv \hat{\tau}_4/\hat{\tau}_2^2, \tag{6.20}$$

are the skewness and kurtosis of FPT. For an autonomous dynamical system, $\mathbf{f} = \mathbf{f}(\mathbf{z}_0)$, the PDF of FPT still varies with time [satisfying the Backward Fokker–Planck equation (6.17)]. However, the first two moments of FPT are given by (Chu *et al*. 2002a,b),

$$\left(\sigma\xi_0 - g\xi_0^2\right)\frac{\mathrm{d}\tau_1}{\mathrm{d}\xi_0} + \frac{q^2\xi_0^2}{2}\frac{\mathrm{d}^2\tau_1}{\mathrm{d}\xi_0^2} = -1, \tag{6.21}$$

$$\left(\sigma\xi_0 - g\xi_0^2\right)\frac{\mathrm{d}\tau_2}{\mathrm{d}\xi_0} + \frac{q^2\xi_0^2}{2}\frac{\mathrm{d}^2\tau_2}{\mathrm{d}\xi_0^2} = -2\tau_1, \tag{6.22}$$

with the boundary conditions,

$$\tau_1 = 0, \ \tau_2 = 0 \qquad \text{for } \xi_0 = \varepsilon; \tag{6.23}$$

$$\mathrm{d}\tau_1/\mathrm{d}\xi_0 = 0, \ \mathrm{d}\tau_2/\mathrm{d}\xi_0 = 0 \quad \text{for } \xi_0 = \xi_{\text{noise}}. \tag{6.24}$$

P1: SJT Trim: 174mm × 247mm Top: 0.553in Gutter: 0.747in
CUUK726-06 cuuk726/Palmer ISBN: 978 0 521 76105 5 July 6, 2009 17:42

The equations for the moments of FPT (6.21) and (6.22) with the boundary conditions (6.23) and (6.24) have analytical solutions,

$$\tau_1(\bar{\xi}_0, \bar{\xi}_{\text{noise}}, \varepsilon) = \frac{2}{q^2} \int_{\bar{\xi}_0}^{1} y^{-\frac{2\sigma}{q^2}} \exp\left(\frac{2\varepsilon g}{q^2} y\right) \left[\int_{\bar{\xi}_{\text{noise}}}^{y} x^{\frac{2\sigma}{q^2}-2} \exp\left(-\frac{2\varepsilon g}{q^2} x\right) \mathrm{d}x \right] \mathrm{d}y, \tag{6.25}$$

$$\tau_2(\bar{\xi}_0, \bar{\xi}_{\text{noise}}, \varepsilon) = \frac{4}{q^2} \int_{\bar{\xi}_0}^{1} y^{-\frac{2\sigma}{q^2}} \exp\left(\frac{2\varepsilon g}{q^2} y\right) \left[\int_{\bar{\xi}_{\text{noise}}}^{y} \tau_1(x) x^{\frac{2\sigma}{q^2}-2} \exp\left(-\frac{2\varepsilon g}{q^2} x\right) \mathrm{d}x \right] \mathrm{d}y, \tag{6.26}$$

where

$$\bar{\xi}_0 = \xi_0/\varepsilon, \quad \bar{\xi}_{\text{noise}} = \xi_{\text{noise}}/\varepsilon$$

are non-dimensional initial-condition error and noise level scaled by the tolerance level ε, respectively. For given tolerance and noise levels (or user input), the mean and variance of FPT can be calculated using (6.25) and (6.26). For the Nicolis error model (6.16) with the same parameter values as in Nicolis (1992),

$$\sigma = 0.64, \quad g = 0.3, \quad q^2 = 0.2. \tag{6.27}$$

Figures 6.5 and 6 show the curve plots of $\tau_1(\bar{\xi}_0, \bar{\xi}_{\text{noise}}, \varepsilon)$ and $\tau_2(\bar{\xi}_0, \bar{\xi}_{\text{noise}}, \varepsilon)$ versus $\bar{\xi}_0$ for four different values of tolerance level, ε (0.01, 0.1, 1 and 2) and four different values of random noise $\bar{\xi}_{\text{noise}}$ (0.1, 0.2, 0.4 and 0.6). The following features are obtained: (a) τ_1 and τ_2 decrease with increasing $\bar{\xi}_0$, which implies that the higher the initial error, the lower the predictability (or FPT) is; (b) τ_1 and τ_2 decrease with increasing noise level $\bar{\xi}_{\text{noise}}$, which implies that the higher the noise level, the lower the predictability (or FPT) is; and (c) τ_1 and τ_2 increase with the increasing ε, which implies that the higher the tolerance level, the longer the FPT is. Note that the results presented in this subsection are for a given value of stochastic forcing ($q^2 = 0.2$) only.

6.6 Stochastic stability

The stochastic stability addresses effects of random perturbations on trajectories of a dynamical system and estimates its stability in terms of probabilistic measures, such as expected values or distribution functions. In general, the stochastic stability differs from the predictability. However, if a time scale quantifies the model predictability, and if this scale indicates the time when the forecast uncertainty exceeds some boundary or when information on the initial condition is lost, the

P1: SJT Trim: 174mm × 247mm Top: 0.553in Gutter: 0.747in
CUUK726-06 cuuk726/Palmer ISBN: 978 0 521 76105 5 July 6, 2009 17:42

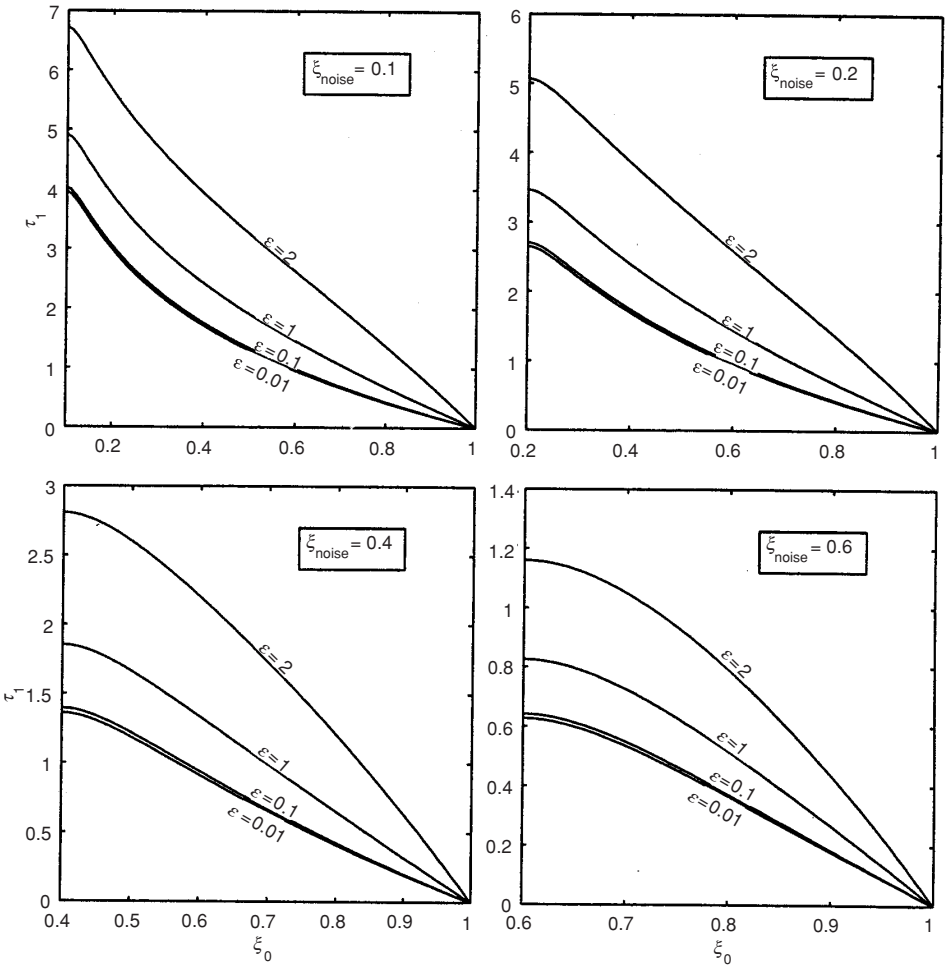

Figure 6.5 Dependence of $\tau_1(\bar{\xi}_0, \bar{\xi}_{\text{noise}}, \varepsilon)$ on the initial condition error $\bar{\xi}_0$ for four different values of ε (0.01, 0.1, 1 and 2) and four different values of random noise $\bar{\xi}_{\text{noise}}$ (0.1, 0.2, 0.4 and 0.6) using the Nicolis (1992) model with stochastic forcing $q^2 = 0.2$ (after Chu *et al*. 2002a).

stochastic stability and predictability are interchangeable. Since these time scales are widely used in meteorology and oceanography, the stochastic stability concept seems to be a useful tool for the predictability analysis of large hydrodynamic models.

Loss of superposition and extreme inhomogeneity are common in nonlinear hydrodynamic models that require local measures of predictability and corresponding timescales (Lorenz 1984). For small-amplitude initial perturbations, the timescales are related to the inverse of the largest Lyapunov exponent estimated by the tangent linear models. The linear approach gives reasonable estimations of

P1: SJT Trim: 174mm × 247mm Top: 0.553in Gutter: 0.747in
CUUK726-06 cuuk726/Palmer ISBN: 978 0 521 76105 5 July 6, 2009 17:42

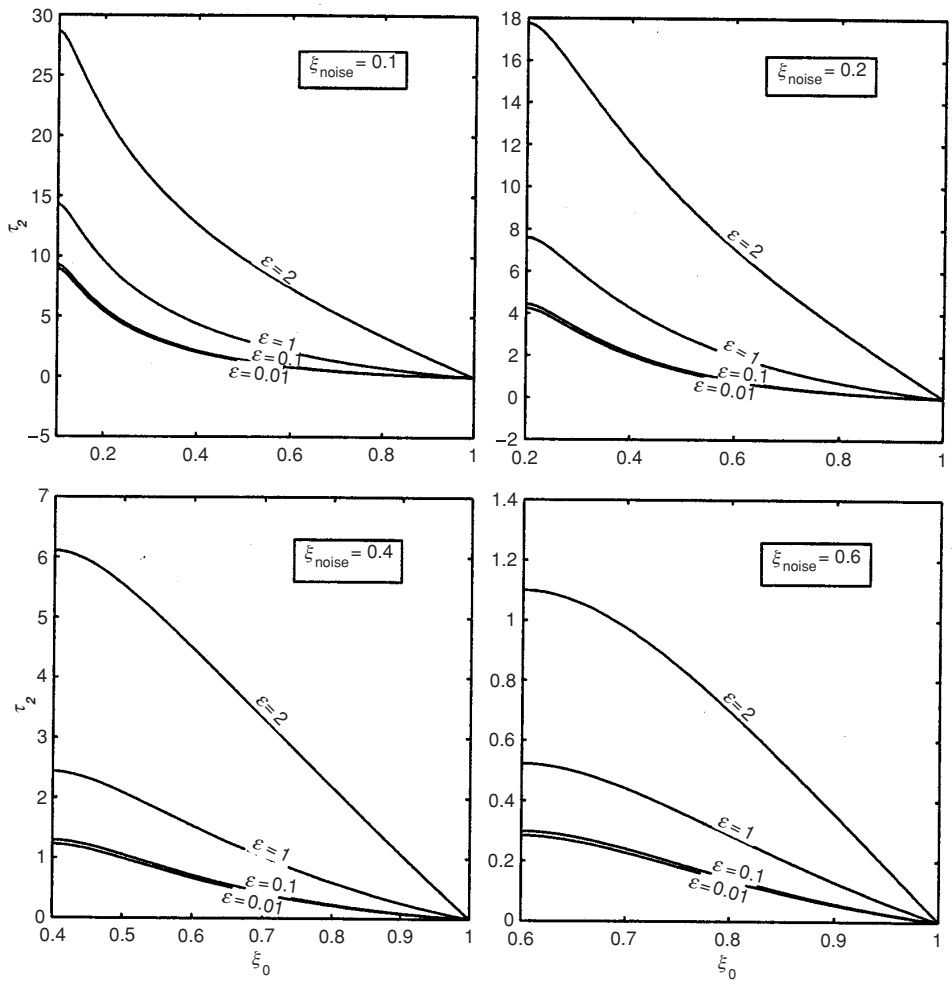

Figure 6.6 Dependence of $\tau_2(\bar{\xi}_0, \bar{\xi}_{\text{noise}}, \varepsilon)$ on the initial condition error $\bar{\xi}_0$ for four different values of ε(0.01, 0.1, 1 and 2) and four different values of random noise $\bar{\xi}_{\text{noise}}$ (0.1, 0.2, 0.4 and 0.6) using the Nicolis (1992) model with stochastic forcing $q^2 = 0.2$ (after Chu *et al*. 2002a).

model predictability in many practical cases. However, it cannot provide critical boundaries on finite-amplitude stability especially in ocean circulation models.

6.6.1 Reference solution

We consider a rectangular semi-closed basin with the horizontal dimensions: $L_1 =$ 1050 km and $L_2 = 1000$ km, and with constant depth $H = 2$ km, which is situated on a mid-latitude β-plane. The basin has rigid (Γ) and open (Γ') boundaries. The

P1: SJT Trim: 174mm × 247mm Top: 0.553in Gutter: 0.747in
CUUK726-06 cuuk726/Palmer ISBN: 978 0 521 76105 5 July 6, 2009 17:42

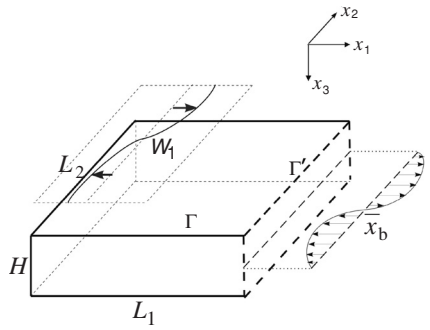

Figure 6.7 Basin geometry. The x_1 and x_2 axes point toward east and north, respectively (after Ivanov and Chu 2007a).

geometry of the basin and its sizes are shown in Fig. 6.7. The numerical model has the nonlinear shallow-water equations with nonlinear bottom friction, wind and boundary forcing

$$\partial Du_1/\partial t + L(Du_2, Du_1) - fDu_2 = -gD\nabla_1\zeta + W_1 - \alpha E^{1/2}u_1, \quad (6.28)$$

$$\partial Du_2/\partial t + L(Du_1, Du_2) + fDu_1 = -gD\nabla_2\zeta + W_2 - \alpha E^{1/2}u_2, \quad (6.29)$$

and the mass conservation equation

$$\partial\zeta/\partial t + (\nabla_1 Du_1 + \nabla_2 Du_2) = 0, \quad (6.30)$$

where $L(\ldots,\ldots)$ is the nonlinear advective operator; $[\nabla_1, \nabla_2] = [\partial/\partial x_1, \partial/\partial x_2]$; u_1 and u_2 are the zonal and meridional velocities, respectively; $D = H + \zeta$, ζ is the sea-surface elevation; the drag coefficient $\alpha = 2.5 \times 10^{-3}$; g is acceleration due to gravity; and $E = u_1^2 + u_2^2$. The Coriolis parameter varies linearly with a beta plane approximation $f = f_0 + \beta x_2$, where $f_0 = 2\Omega\sin(\varphi_0)$ and $\beta = (2\Omega/a)\cos(\varphi_0)$. Here, Ω and a are the rate of rotation and the radius of the Earth, respectively; $\varphi_0 = 35^0$; for the chosen model parameters: $f_0 = 7.3 \times 10^{-5}$ s^{-1}, $\beta = 2.0 \times 10^{-11}$ m^{-1} s^{-1}. A flow in the semi-closed basin bounded by $\Gamma \cup \Gamma'$ is forced by both the zonal wind forcing $W_1 (W_2 = 0)$ varying with latitude as

$$W_1 = -\frac{w_s}{\rho_w}\cos\left(\frac{\pi x_2}{L_2}\right), \quad (6.31)$$

where $\rho_w = 1025$ kg m^{-3}, w_s is the wind stress, $w_s/\rho_w = 1.0 \times 10^{-3}$ m^2 s^{-2}, and a prescribed net flux [characterised by the normal velocity $\bar{u}_b(x_2, t)$ and surface elevation $\bar{\varsigma}_b(x_2, t)$ along the boundary Γ'].

Zero normal velocity and zero Neumann conditions for the surface elevation are imposed on the rigid boundary Γ. The chosen model configuration is suitable for the analysis of ocean model predictability affected by different kinds of stochastic

P1: SJT Trim: 174mm × 247mm Top: 0.553in Gutter: 0.747in
CUUK726-06 cuuk726/Palmer ISBN: 978 0 521 76105 5 July 6, 2009 17:42

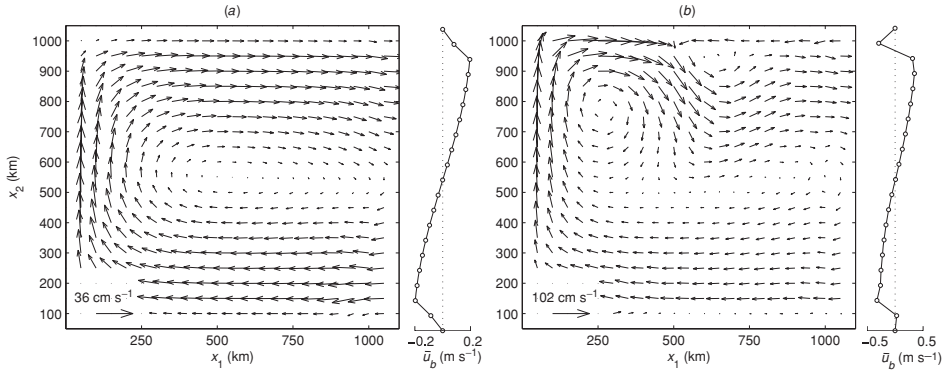

Figure 6.8 Spatial structure of the reference solution at the initial state (*a*) and after integration for 60 days (*b*). Open boundary conditions ($\bar{u}_b$) corresponding to the reference solution are shown to the right of the circulation patterns (after Ivanov and Chu 2007a,b).

uncertainties: errors inserted in initial conditions (Ivanov and Chu 2007a,b), wind (the present study) and open boundary conditions. Cross-correlations between these errors can also be studied. Model (6.28)–(6.30) is similar to that used by Veronis (1966) for the analysis of nonlinear wind-driven circulation in a closed basin. But in contrast to *Veronis* (1966) we parameterise bottom friction by the quadratic drag law.

The prescribed non-stationary net flux across the open boundary is computed as explained in Chu *et al*. (1997). The structure of open boundary conditions on day-0 and day-60 is demonstrated in Figs. 6.8*a* and 6.8*b*, respectively. The initial condition represents a non-closed anticyclonic gyre shown in Fig. 6.8*a*. The corresponding initial surface elevation is not shown because its structure is obvious. After 30 days of integration the model reaches a spin up when the spatially averaged kinetic energy oscillates with a period of 120 days. Amplitude of this oscillation reduces with time exponentially with rate of 1000 d^{-1}. The circulation pattern formed after day-30 presents a multigyre structure with maximum velocities up to 0.9 to 1.0 m s^{-1} (Fig. 6.8*b*).

6.6.2 Ensemble prediction

For simplicity, Ivanov and Chu (2007a,b) sampled perturbations from specified, multivariate normal distributions. First, due to simplicity, our hydrodynamic model is able to produce forecast ensembles containing up to $\sim O(10^5)$ perturbations. Second, the Latin hypercube (LHC) design (Latin Hypercube; see http://www.mathworks.com/matlabcentral/fileexchange/4352) was applied to simulate a highly uniform distribution of an initial error in the phase space. Using

P1: SJT Trim: 174mm × 247mm Top: 0.553in Gutter: 0.747in
CUUK726-06 cuuk726/Palmer ISBN: 978 0 521 76105 5 July 6, 2009 17:42

pure probabilistic arguments, Downing *et al*. (1985) pointed out that the Latin hypercube design is more effective than the classical Monte-Carlo method. For obtaining dense error coverage with the same degree of homogeneity from Monte-Carlo samples and through the LHC design N^{M_0} and $N(2M_0 + 2)$ statistical realisations are required, respectively. Here, N is the number of statistical realisations necessary to simulate one degree of freedom, and M_0 is the truncated mode number. Typically, $N \sim O(10^3)$. For $M_0 = 15$, the classical Monte-Carlo method requires $\sim O(10^{45})$ initial perturbations for a statistically significant estimate. This is not feasible with available computer resources. Comparable results can be obtained by the LHC design approach with only $\sim O(10^4)$ initial perturbations.

The LHC design approach provides the dense error coverage of the model phase space for $\sim O(10^4)$ initial perturbations. This number of initial perturbations is a trade-off between the ensemble ability to reproduce the main features of IE statistics, and the computational cost. However, the optimal number of initial perturbations (N_{opt}) should be specified for the concrete ocean model. We estimated this number through the Kullback–Leibler (KL) distance (the relative entropy; see White 1994).

The KL distance is a natural distance function from a 'true' probability density, F_∞, to a 'target' probability density, F_N. For continuous density functions, the KL distance is defined as

$$KL_N(F_\infty | F_N) = \int_0^\infty d\tau F_N(\tau) \log\left[\frac{F_\infty(\tau)}{F_N(\tau)}\right], \tag{6.32}$$

where $F_N(\tau)$ and $F_\infty(\tau)$ are τ-PDFs computed for an N sample ensemble and a hypothetic ensemble with infinite sampling, respectively. In practice, a difference between two distributions is negligible if $KL_N \leq 5.0 \times 10^{-3}$ (White 1994).

To calculate the KL distance we suppose $F_\infty = F_{100000}$ because only small differences in τ-statistics estimated from ensembles of 5.0×10^3, 1.0×10^4, 2.0×10^4, 5.0×10^4 and 1.0×10^5 samples have been observed. The KL_N rapidly reduces with N from 2.0×10^{-1} ($N = 20$) to 4.0×10^{-3} ($N = 10^3$). Therefore, N_{opt} was chosen as 10^3.

6.6.3 Stochastic perturbations

Two types of (stochastic) initial perturbations are introduced: two-dimensional isotropic Gaussian white noise [white-noise-like perturbations (WNLPs)] with the two-point correlation function

$$\langle u_i'(\mathbf{x}) u_j'(\mathbf{x}')\rangle = I^2 \delta_{ij} \delta(\mathbf{x} - \mathbf{x}'), \tag{6.33}$$

P1: SJT Trim: 174mm × 247mm Top: 0.553in Gutter: 0.747in
CUUK726-06 cuuk726/Palmer ISBN: 978 0 521 76105 5 July 6, 2009 17:42

or two-dimensional isotropic Gaussian spatially correlated noise [red-noise-like perturbations (RNLPs)] with the two-point correlation function

$$\langle u_i'(\mathbf{x}) u_j'(\mathbf{x}') \rangle = I^2 \delta_{ij} \exp\left[-\frac{(\mathbf{x} - \mathbf{x}')^2}{2R_\perp{}^2} \right], \tag{6.34}$$

where $\mathbf{x} = (x_1, x_2)$, $R_\perp$, I^2 are correlation radius and noise variance (intensity of perturbations), respectively. These perturbations are directly added to the initial conditions. The technical details of generating Gaussian noises with correlation functions (6.33) and (6.34) can be found in Sabel'feld (1991). The non-dimensional intensity of the initial perturbations $\bar{I}^2 = (I/I_0)^2 (I_0 = 1\ \mathrm{m\,s^{-1}})$ will be used below. Noise with correlation functions (6.33) and (6.34) is the popular model of errors for optimal interpolation or spline fitting. Both of these procedures are applied to construct initial conditions for ocean models from irregularly spaced data (Brasseur *et al*. 1996).

The stochastic wind perturbation $\mathbf{U}$ is represented by (Sura *et al*. 2001)

$$\mathbf{U} = [U_1(x_1, x_2, t), U_2(x_1, x_2, t),] = \boldsymbol{\mu}(t)\sigma \quad G^{1/2}(x_1, x_2), \tag{6.35}$$

where $\boldsymbol{\mu}(t) = [\mu_1(t), \mu_2(t)]$ are white Gaussian vector processes with zero mean and unit variance; σ^2 is the wind variance; the spatial structure function G characterises a degree of spatial inhomogeneity of wind perturbations above an area of interest. Two different structure functions G are used. The first one is given by

$$G_1(x_1, x_2) = \cos\left(\frac{\pi x_2}{L_2} \right). \tag{6.36}$$

In this case only the amplitude of wind stress (6.33) is distorted by the non-Gaussian white noise. The second one is chosen as

$$G_2(x_1, x_2) = \alpha_s \left[\pi \beta_1 \beta_2 \mathrm{erf}\left(\frac{L_1}{2\beta_1} \right) \quad \mathrm{erf}\left(\frac{L_2}{2\beta_2} \right) \right]^{-1/2}$$

$$\times \exp\left(-\frac{(x_1 - L_1/2)^2}{2\beta_1^2} - \frac{(x_2 - L_2/2)^2}{2\beta_2^2} \right). \tag{6.37}$$

Here, erf is the error function; α_s is a scaling parameter; (β_1, β_2) are the decorrelation scales; G_2 shows the impact of the localised atmospheric eddy activity near the point $(L_1/2, L_2/2)$ on the surface wind perturbations with $\beta_c = \beta_1 = \beta_2 =$ 600 km (Sura *et al*. 2001). In most numerical experiments the scaling constant α_s is chosen to adjust the weight function in (6.13) to 1. However, a number of computations use β_c between 100 km and 600 km. The noise in the surface wind with $\sigma^2 = 28.0\ \mathrm{m^2\ s^{-2}}$ corresponds to typical observed atmospheric conditions in

P1: SJT Trim: 174mm × 247mm Top: 0.553in Gutter: 0.747in
CUUK726-06 cuuk726/Palmer ISBN: 978 0 521 76105 5 July 6, 2009 17:42

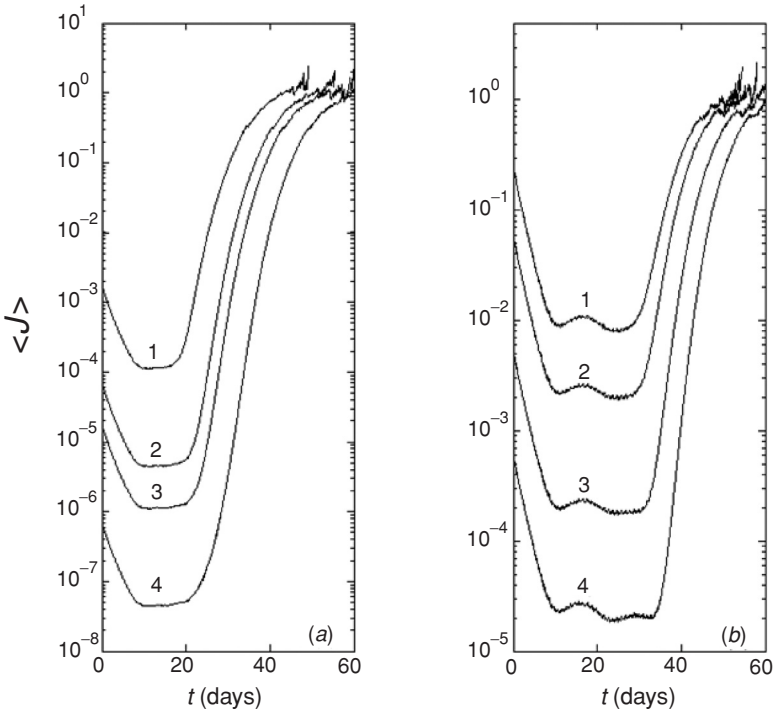

Figure 6.9 Temporal evolution of the root mean square error $<J>$ for various initial perturbations: (a) WNLPs with different noise intensities: 0.05, 0.01, 0.005 and 0.001 (denoted by '1', '2', '3', '4'); and (b) RNLPs with the correlation radius of 70 km and different noise intensities: 0.02, 0.01, 0.003 and 0.001 (denoted by '1', '2', '3', '4') (after Ivanov and Chu 2007a).

the North Atlantic region (Wright 1988). Therefore, the stochastic forcing (6.35)–(6.37) is a conceptual tool to study the effect of noise on simple and more complex wind-driven regional ocean models.

6.6.4 Stability due to initial uncertainty

At least four stages for the IE evolution are identified for both WNLPs (Fig. 6.9*a*) and RNLPs (Fig. 6.9*b*). All these stages are clearly identified by the IE growth rate. Initial error decay is observed for the first ten days of IE evolution (Figs. 6.9*a*,*b*) where the IE growth rate, $Q \equiv \mathrm{d}\ln\langle J\rangle/\mathrm{d}t$, evolves as

$$Q \approx Q_0[\exp(\alpha_0 t) - \alpha_1], \tag{6.38}$$

where α_0 is the decay exponent, $Q_0 \approx -0.45$, $\alpha_0 = \ln \alpha_1/t_1$, $t_1 = 10$ d.

Non-exponential initial error decay corresponding to (6.38) differs from a quasi-exponential decay obtained in Wirth & Ghil's (2000) model with the dissipative

P1: SJT Trim: 174mm × 247mm Top: 0.553in Gutter: 0.747in
CUUK726-06 cuuk726/Palmer ISBN: 978 0 521 76105 5 July 6, 2009 17:42

operator $\nu\Delta_\perp$ and quite large horizontal viscosity ν. In contrast to this model the zero horizontal viscosity is used in our model. Therefore, the non-exponential decay seems to be caused by nonlinear bottom friction. Then $\langle J(t)\rangle$ has quasi-stationary low values during 10 and 20 days for WNLPs (Fig. 6.9*a*) and RNLPs (Fig. 6.9b), respectively. During the third stage (after day-20 and day-30 for WNLPs and RNLPs, respectively) the IE grows faster than exponentially (Figs. 6.9*a*,*b*).

Linear theory suggests that the larger the amplitude of the initial perturbations, the higher the probability of obtaining low model predictability. The IE should steadily increase with a prediction time scale in the linear predictability regime. In contrast to this, forecast skill may decay more slowly when the amplitude of initial perturbations increases. The growing perturbations rapidly adopt a horizontal scale comparable to that of the reference state (linear predictability regime), and further growth is limited by interactions with this state and among them (nonlinear predictability regime). In the nonlinear predictability regime the IE demonstrates clear contributions from the cumulative effects of flow scales, and the predictability time is no longer measured by the inverse of the leading Lyapunov exponent. Moreover, model predictability is enhanced with the growth of the correlation radius $R_\perp$ and is less sensitive to the choice of the intensity $\bar{I}^2$.

Ivanov and Chu (2007a) demonstrated the existence of the linear predictability regime identified by non-Gaussian statistics and (quasi)-exponential growth of prediction error, for a small correlation radius ($R_\perp \ll 50$ km, in the case of WNLPs) and large noise intensities ($\bar{I}^2 \leq 0.2$). For WNLPs, the typical τ-PDF was close to Gaussian if $\bar{I}^2 \sim 0.01$–0.05. The growth of $\bar{I}^2$ up to 0.1–0.2 resulted in a weak asymmetry for the τ-PDF (SK $\rightarrow$ 0.15) and departs from non-Gaussian (KU $\rightarrow$ 3.10). However, although such a τ-PDF has a short tail (labelled '1' in Fig. 6.10*a*), it was still close to Gaussian and the mean τ-IPT reduced with the growth in amplitude of initial perturbations. The τ-PDF quickly departs from Gaussian with the growth of $\bar{I}^2$ after 0.2. However, from a physical point of view, such initial perturbations seem to be too large to exist in reality.

The nonlinear predictability regime appears as $R_\perp$ grows. Both highly non-Gaussian τ-PDFs, and the mean FPT that grows with increasing $R_\perp$, indicate that the PE becomes nonlinear. A typical non-Gaussian τ-PDF (SK ≈ 0.8, KU ≈ 4.0) computed for a finite correlation radius is demonstrated in Fig. 6.10*b*. The long PDF tail (labelled '2' in Fig. 6.10*b*) is clearly seen in this figure. The tail is formed by rare individual forecasts (FPT up to 60 days), each of which is longer than the mean ensemble forecasting (FPT of about 44 days).

The first four parameters of FPT were computed for various values of correlation radius $R_\perp$. The asymmetry of τ-PDFs becomes higher for the larger values of correlation radius $R_\perp$ (Fig. 6.11). The SK value, which is a measure of asymmetry, increases up to 0.8 when $R_\perp$ tends to 100 km. Larger values of mean FPT

P1: SJT Trim: 174mm × 247mm Top: 0.553in Gutter: 0.747in
CUUK726-06 cuuk726/Palmer ISBN: 978 0 521 76105 5 July 6, 2009 17:42

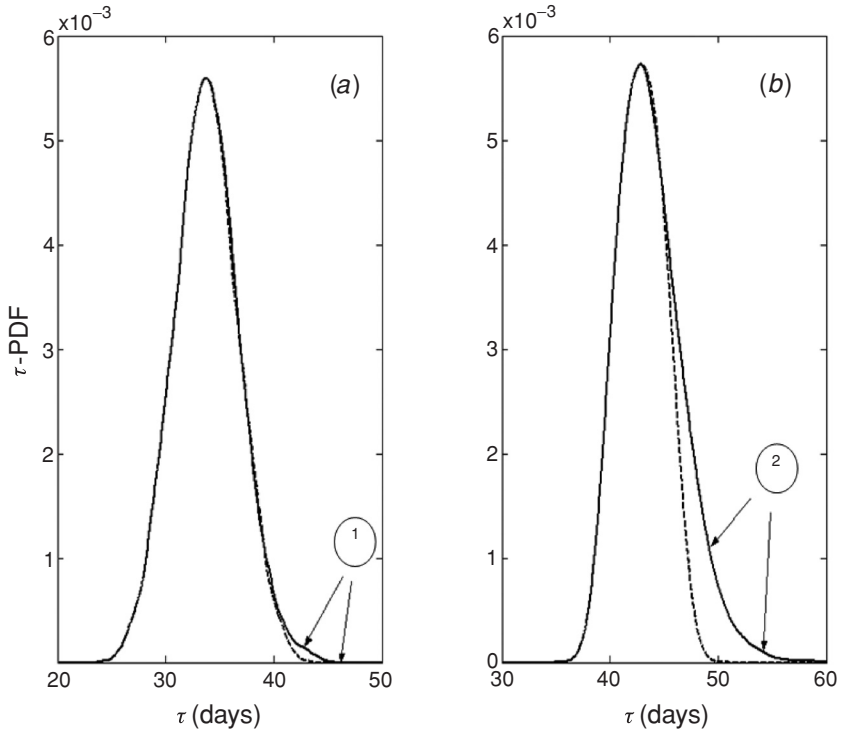

Figure 6.10 The τ-PDFs for (*a*) WNLPs with $\bar{I}^2 = 0.1$, $R_\perp = 30$ km and $\bar{\varepsilon}^2 = 0.5$; and (*b*) RNLPs with $\bar{I}^2 = 0.1$, $R_\perp = 125$ km and $\bar{\varepsilon}^2 = 0.2$. Skewness and kurtosis are 0.15 and 3.09 for (*a*), and 0.77 and 3.95 for (*b*). Dashed lines indicate mirror reflections of the left-hand-side tails of τ-PDFs (from Ivanov and Chu 2007a).

(Fig. 6.11*a*) and τ-variances (Fig. 6.11*b*) correspond to more asymmetric PDFs. Highly non-Gaussian (KU ≈ 4, Fig. 6.11*d*) and sharp τ-PDFs with long tails stretching to large prediction times accompany this nonlinear predictability regime. The explicit growth of mean predictability time observed with the growth of correlation radius $R_\perp$ is strong evidence of the nonlinear predictability regimes caused by the inhomogeneous morphology of the model phase space (Kaneko 1998).

6.6.5 Stability due to surface wind uncertainty

Perturbations excited by uncertain winds grow at all scales and during the whole 50–60 day period. This is in contrast to the case when there is uncertainty in the initial condition only. Therefore, the presence of the spatio-temporal noise (6.34) in wind forcing (6.33) causes the monotonic error growth. At least four predictability regimes are identified from Fig. 6.12. In all the cases the IE grows in a monotonic manner but with different speeds. More accurately, these regimes can be identified

P1: SJT Trim: 174mm × 247mm Top: 0.553in Gutter: 0.747in
CUUK726-06 cuuk726/Palmer ISBN: 978 0 521 76105 5 July 6, 2009 17:42

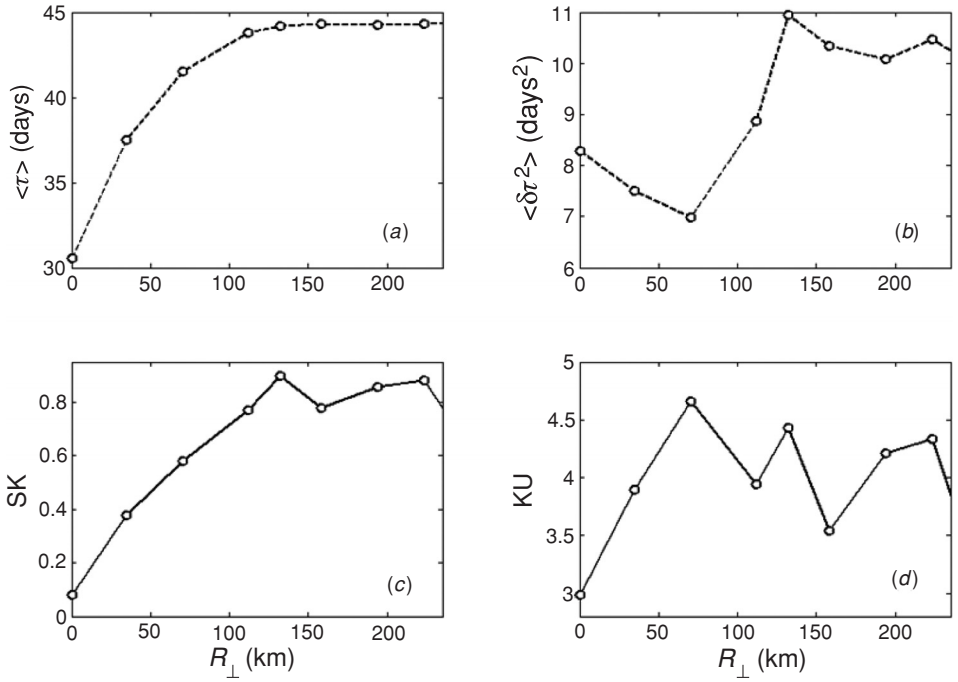

Figure 6.11 Dependence of τ-statistics on the correlation radius for RNLPs with the noise intensity of 0.1, and tolerance level 0.2: (*a*) τ-mean, (*b*) τ-variance, (*c*) τ-skewness, (*d*) τ-kurtosis (after Ivanov and Chu 2007a).

using the error growth rate (Q): linear growth, power growth and super-exponential growth.

The error dynamics strongly depends on the intensity and spatial inhomogeneity of wind uncertainty (G, $\bar{\sigma}^2$) as shown in Fig. 6.12. During the linear error growth, mean square IE is represented by,

$$\langle J \rangle \approx D_{\text{eff}} t, \tag{6.39}$$

Duration of the linear IE growth regime is typically up to 4–5 days if $\bar{\sigma}^2 \sim 0.1$–1.0. The effective coefficient D_{eff} is determined by summation of contributions from the error source term at all wavenumbers (Ivanov & Chu 2007b). The linear law (6.39) was earlier documented in a number of studies (see, for example Vannitsem and Toth 2002, personal communication). However, Ivanov & Chu (2007b) analytically determined the error sources with strong dependence on the effective coefficient on the variance of wind as well as on the degree of spatial inhomogeneity of the wind forcing.

For moderate but inhomogeneous winds, Ivanov and Chu (2007b) found the power growth of perturbations after the transient phase (for example, see Fig. 6.12).

P1: SJT Trim: 174mm × 247mm Top: 0.553in Gutter: 0.747in
CUUK726-06 cuuk726/Palmer ISBN: 978 0 521 76105 5 July 6, 2009 17:42

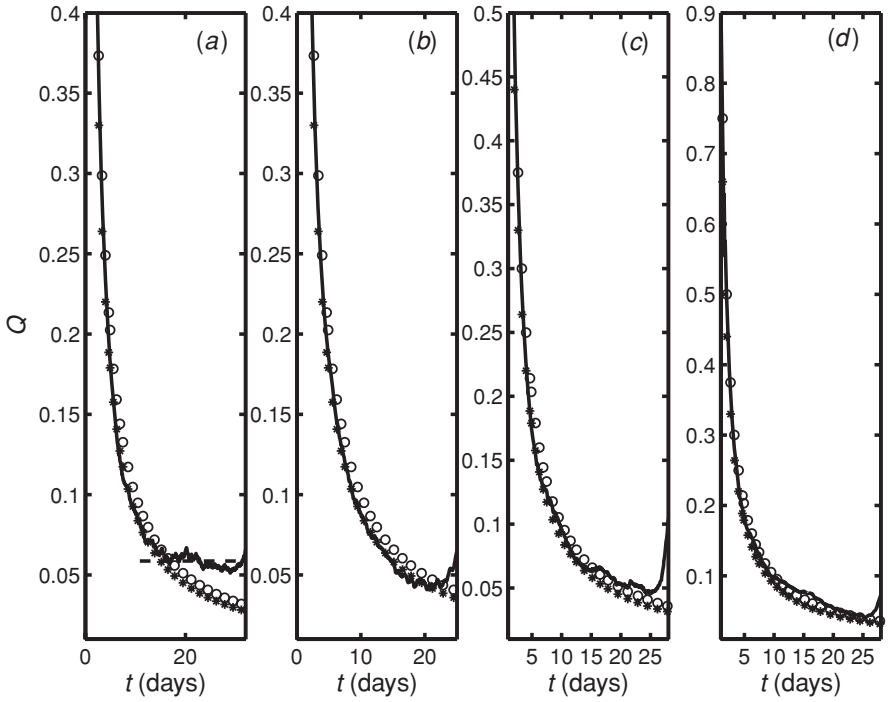

Figure 6.12 The growth rate Q (solid curve) for different $\bar{\sigma}^2$ and G: (*a*) $\bar{\sigma}^2 = 0.1$, $G = G_2$; (*b*) $\bar{\sigma}^2 = 1.0$, $G = G_1$; (*c*) $\bar{\sigma}^2 = 1.0$, $G = G_2$, and (*d*) $\bar{\sigma}^2 = 2.0$, $G = G_2$. The solid curve, white dots and asterisks show exponential, linear and power (with scaling exponent of 8.8×10^{-1}) laws, respectively (after Ivanov and Chu 2007b).

For small values of $\bar{\sigma}^2 \ll 1.0$ the power growth is replaced by exponential growth (shown by the dashed line in Fig. 6.12*a*).

If $\bar{\sigma}^2$ exceeds 1, there is no exponential growth and the IE grows with the power law the power exponent being about 8.8×10^{-1}. This regime exists between day-5 and day-15 in Fig. 6.12*a*, between day-7 and day-23 in Fig. 6.12*b*, between day-4 and day-14 in Fig. 6.12*c*, but there is no power-law regime in Fig. 6.12*d* when the stochastic wind uncertainty is too large ($\bar{\sigma}^2 > 2.0$). For such a variance the linear growth of IE dominates. Smaller scales affected by the stochastic wind are subject to strong viscous damping due to the increasing drag coefficient α with the growth of kinetic energy of large-scale perturbations. Therefore, the smaller scales grow more slowly than the unstable large scales. The growing perturbations rapidly adopt the horizontal scales comparable to those of the reference state. Alternatively, stronger stochastic wind ($\bar{\sigma}^2 \geq 1.0$) excites more modes at smaller scales than weak wind, and the coherent behaviour of the modes is clearly observed in this case (for example see Fig. 6.12*b*).

P1: SJT Trim: 174mm × 247mm Top: 0.553in Gutter: 0.747in
CUUK726-06 cuuk726/Palmer ISBN: 978 0 521 76105 5 July 6, 2009 17:42

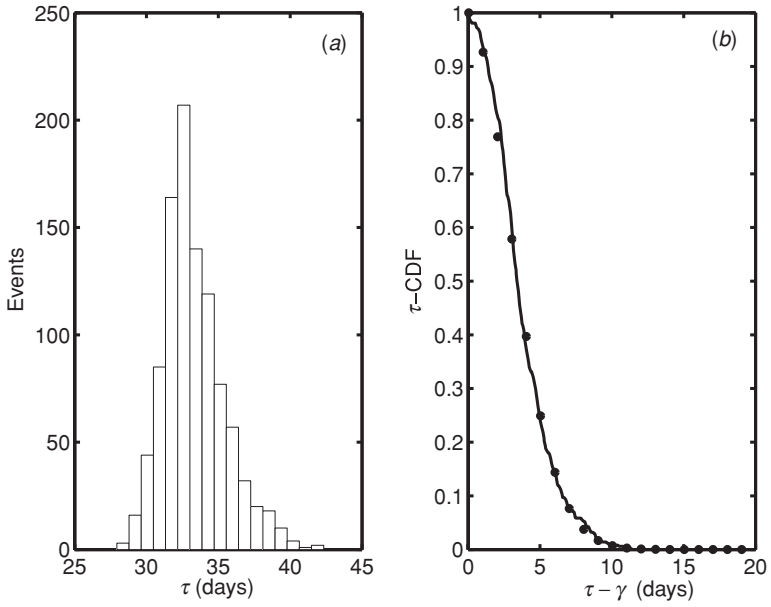

Figure 6.13 Identification of τ-CDF: (a) FPT histogram for a 103-term ensemble; (*b*) CDF computed directly from the ensemble (solid curve) and using the developed method (black dots), $\gamma = 30$ days (after Ivanov and Chu 2007b).

For finite-amplitude IEs, stochastic wind forcing (6.10), in general, induces highly non-Gaussian τ-PDFs. The following question arises: what kind of statistics can be used to represent such τ-PDFs? If an appropriate distribution function is found, it would be possible to identify the ensemble-generated PDFs from a limited observation series and small forecast ensembles, and in turn to estimate the model predictability horizon. Ivanov and Chu (2007b) found that the FPT satisfies the three-parameter Weibull distribution (Fig. 6.13*a*)

$$f(\tau) = \frac{\beta}{\eta}\left(\frac{\tau-\gamma}{\eta}\right)^{\beta-1} \exp\left[-\left(\frac{\tau-\gamma}{\eta}\right)^{\beta}\right], \tag{6.40}$$

with (η, γ, β) the scale, shape and location parameters, which were estimated by an algorithm on the basis of the Kullback–Leibler distance (White 1994). The τ-CDFs computed by the non-parametrical technique (solid curve) and our method (black dots) are compared in Fig. 6.13*b*. The parameters (η, γ, β) have the values 3.71, 30.0 and 1.67 days, respectively. The parameter β affects the length of the PDF tail formed by rare forecasts, which are longer than the mean ensemble forecast $\langle\tau\rangle$. A small value of β indicates an enhanced probability for the realisation of abnormally long (in our case up to 50 days) model forecasts.

P1: SJT Trim: 174mm × 247mm Top: 0.553in Gutter: 0.747in
CUUK726-06 cuuk726/Palmer ISBN: 978 0 521 76105 5 July 6, 2009 17:42

6.7 Power decay law

A random process is called fractional Brownian motion if its cumulative FPT density function satisfies the power law (Ding and Yang 1995),

$$P(\tau) \sim \tau^{H-1}, \tag{6.41}$$

with $0 < H < 1$. Here H is the Hurst exponent. For $H = 1/2$, the random process is the ordinary Brownian motion.

The cumulative distribution, $P(\tau_\rho)$, for each climate index datum (Fig. 6.14) shows a power-law feature in the tail of the distribution scales. For a very small value of the index reduction, ρ_0 (0.01 for the AO, AAO, NAO and PNA indices and 0.1 for SOI), the cumulative FPT density function calculated from the index data shows that

$$P(\tau_0) \sim \tau_0^{-\alpha_0}, \tag{6.42}$$

with $\alpha_0 \sim 1/2$. Since the Hurst exponent of an ordinary Brownian motion is $H = 1/2$, the empirically observed scaling (Fig. 6.14) is a consequence of the (at least close to) Brownian motion behaviour of the climate indices.

This argument of an unbiased Brownian motion is also strengthened by observing that (Fig. 6.14)

$$P(\tau_0 = 1) \sim 1/2. \tag{6.43}$$

This indicates that the climate index has a 50% chance of increase and decrease at each time step (one month). Figure 6.14 also shows the cumulative distributions $P(\tau_\rho)$ for different values of ρ, i.e. $\rho = 0.01$, 0.5, 1.0, and 1.5 for the (AO, AAO, NAO, PNA) indices and $\rho = 0.1$, 10, 20, and 30 for SOI. From this figure it is seen that the tail exponent, α_ρ, is rather insensitive to the value of ρ. In particular one finds that $\alpha_\rho \sim 1/2$ over a broad range of values for ρ, a value that is consistent with the Brownian motion hypothesis.

Such a power decay law in FPT is also found in model predictability. The Gulf of Mexico real-time nowcast/forecast system is taken as an example to show the existence of the power decay law of FPT in the predictability skill. This system (Chu *et al*. 2002c) was built based on the Princeton Ocean Model (POM) with $1/12^\circ \times 1/12^\circ$ horizontal resolution. Real-time sea-surface height (SSH) anomalies derived from NASA/CNES TOPEX and ESA ERS-2 altimeters, and composite SST data derived from the NOAA Advanced Very High Resolution Radiometer (AVHRR) in a continuous data assimilation mode are used to produce a nowcast and four-week forecast. It was found that the forecast retains considerable skill to about one-two weeks, beyond which it begins to deviate rapidly from reality.

The Gulf of Mexico velocity data at 50 m depth are archived every six hours from the nowcast/forecast system for six months beginning on 9 July 1998. The

P1: SJT Trim: 174mm × 247mm Top: 0.553in Gutter: 0.747in
CUUK726-06 cuuk726/Palmer ISBN: 978 0 521 76105 5 July 6, 2009 17:42

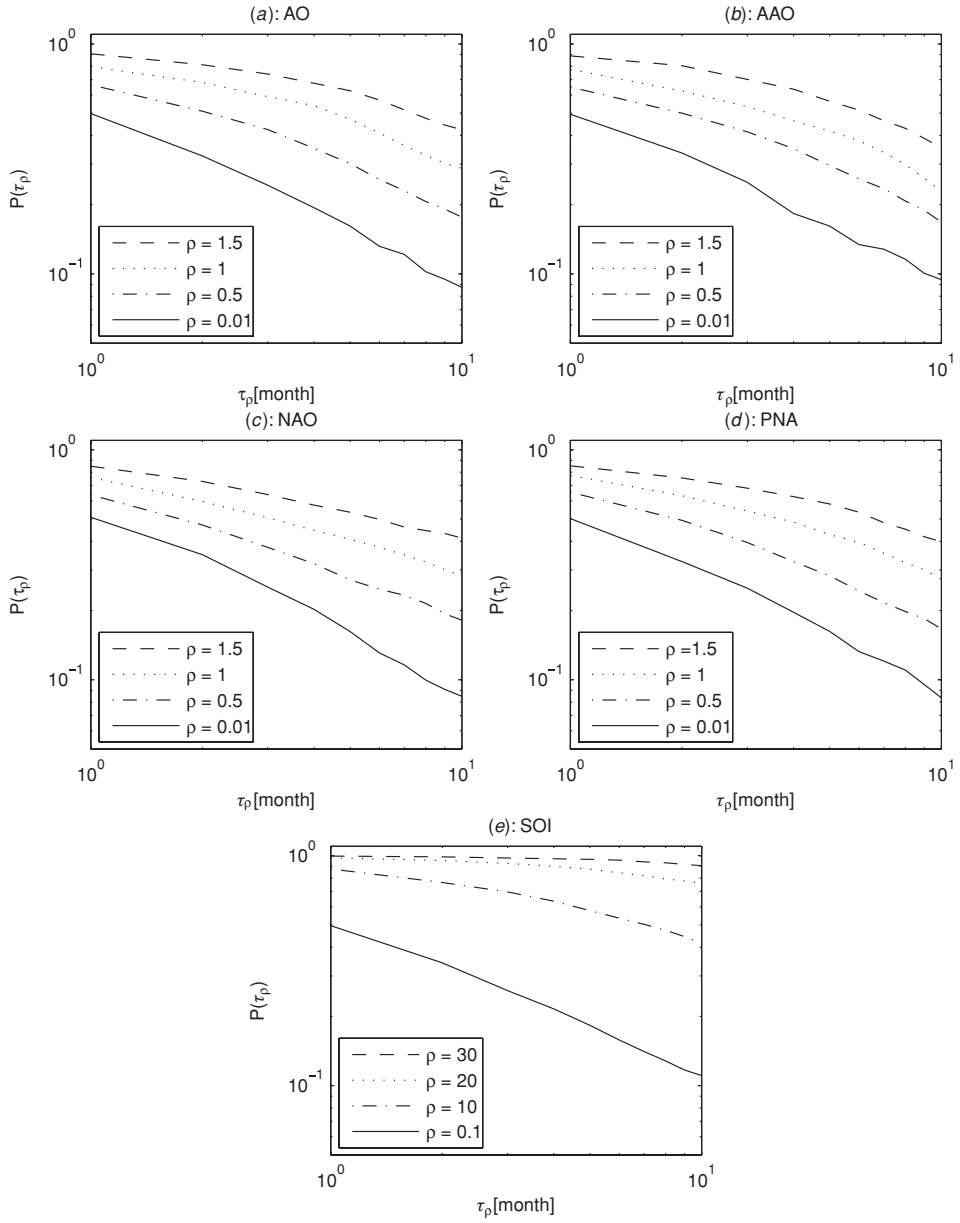

Figure 6.14 The empirical cumulative density functions, $P(\tau_\rho)$, for different values of the index reduction for (*a*) Arctic Oscillation (AO), (*b*) Antarctic Oscillation (AAO), (*c*) North Atlantic Oscillation (NAO), (*d*) Pacific–North American Pattern (PNA) and (*e*) Southern Oscillation (SO). It shows the power-law features (after Chu 2008).

P1: SJT Trim: 174mm × 247mm Top: 0.553in Gutter: 0.747in
CUUK726-06 cuuk726/Palmer ISBN: 978 0 521 76105 5 July 6, 2009 17:42

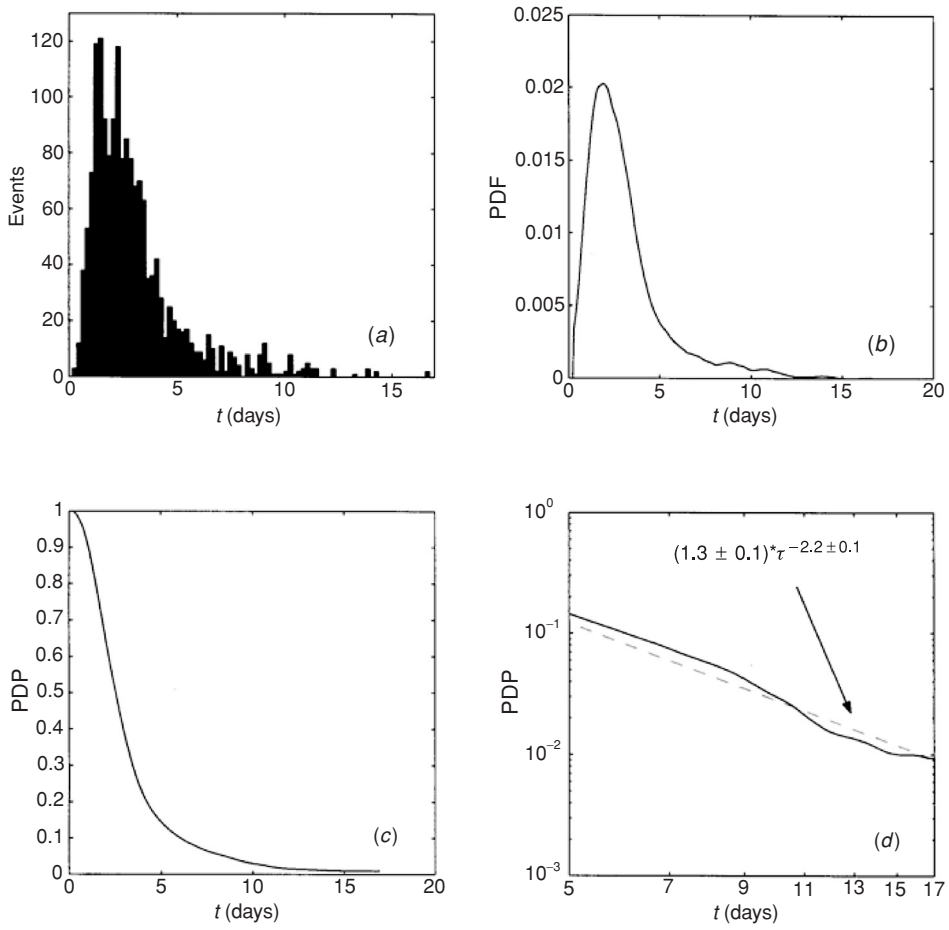

Figure 6.15 Statistical characteristics of VPP for zero initial error and 55 km tolerance level: (*a*) histogram of FPT, (*b*) PDF of FPT computed using the Epanechnikov kernel density, (*c*) PDP for FPT between 0 and 20 days, and (*d*) PDP for FPT between 5 and 17 days (after Chu *et al*. 2002c).

observational data are collected from 50 satellite-tracked drift buoys at 50 m depth. Since the number of drift buoys is limited (50 in this study), the point stochastic process is used to create more realisations to calculate the ensemble mean of the predictability skill (Tikhonov & Khomenko 1998). Moving along the drifter trajectory $\mathbf{y}(t)$, points are randomly selected and the predictability skill is calculated for each of these points. Such a process is called the point stochastic process. The average over these points is equivalent to the ensemble average due to the ergodic feature of the trajectories (Dymnikov & Filatov 1987; Tikhonov & Khomenko 1998).

The FPT is computed for non-ensemble prediction with a tolerance level (ε) of 55 km and without initial error ($\mathbf{z}_0 = 0$). The PDF of FPT (Fig. 6.15), calculated

P1: SJT Trim: 174mm × 247mm Top: 0.553in Gutter: 0.747in
CUUK726-06 cuuk726/Palmer ISBN: 978 0 521 76105 5 July 6, 2009 17:42

using the Epanechnikov kernel density (Good 1996) from the histogram (Fig. 6.15*a*), shows a non-Gaussian distribution with a narrow peak and a long tail in the domain of long-term prediction. Successful 10–15 day predictions are abnormally long (called the extreme long predictions) compared to the mean FPT (3.2 days) and the most probable FPT (2.4 day). The tail of the probability density of prediction follows the power law 5 with the power exponent, $\gamma = 2.2$ (Figs. 6.15*c* and *d*).

6.8 Lagrangian predictability

During the World Ocean Circulation Experiment (WOCE), the ocean velocity observation has been significantly advanced with extensive spatial and temporal coverage using near-surface Lagrangian drifters, RAFOS floats and Autonomous Lagrangian Circulation Explorers (ALACEs). Trajectories of these quasi-Lagrangian drifters reflect the whole spectrum of ocean motions, including meso- and submeso-scale eddies, various waves, inertial and semi-diurnal motions, and provide invaluable resources to estimate the forecast skill. However, direct comparison between model and Lagrangian observational data is difficult since neither the dynamics of numerical models nor their forcing data (such as surface forcing functions) are identical to the reality. It needs to be determined if the model–data difference comes from a deficiency in modelling ocean physics, from some unessential imperfection or from unrepresentative data. It is clear that the high-resolution ocean model and the Lagrangian drifter data are compared only in the statistical sense. Since the mesoscale (10–50 km) movements of Lagrangain drifters represent the eddy dynamics, it is reasonable to ask if the high-resolution ocean model reproduces the mesoscale Lagrangian drifter movements. Such a model capability, defined as the 'Lagrangian predictability' (Mariano *et al*. 2002) as distinct from the 'Eulerian predictability' has the capability to reproduce patterns and topological details of the circulation attractor.

The Lagrangian data were collected from 15 satellite-tracked sonobuoys, manufactured by the Applied Technology Associates and deployed by Horizon Marine, provided the Lagrangian data used for the study. A nylon drogue at 50 m depth is tethered to the buoy hull of which 0.64 m is in the water and 0.33 m in the air. The drifter trajectories used in the present study are given in Fig. 6.16. The synthetic particle trajectories are obtained from the time integration of the modelled horizontal velocity field at 50 m depth with bi-cubic spline interpolation in space and second-order interpolation in time.

The PDF of FPT for zero initial errors is calculated from the drifter and synthetic particle trajectories with four tolerance levels (ε) (0.25°, 0.5°, 0.75° and 1.25°). It clearly shows non-Gaussian distribution (Fig. 6.17). The long tail stretching

P1: SJT Trim: 174mm × 247mm Top: 0.553in Gutter: 0.747in
CUUK726-06 cuuk726/Palmer ISBN: 978 0 521 76105 5 July 6, 2009 17:42

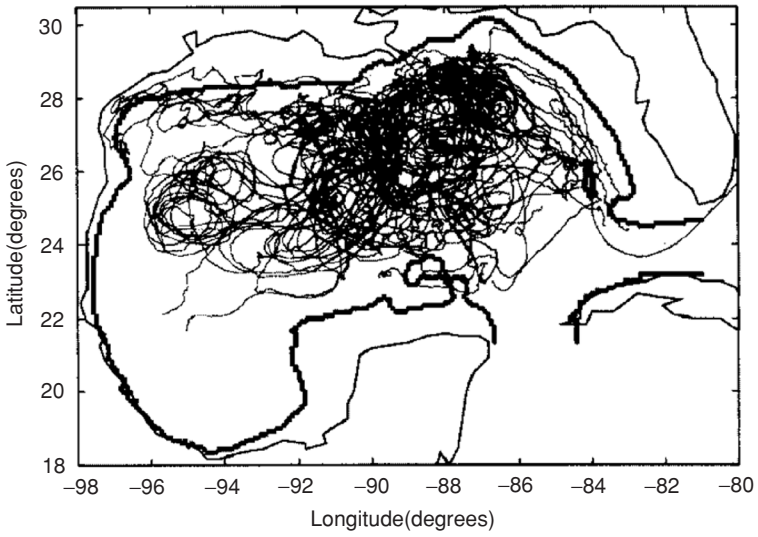

Figure 6.16 Spaghetti of 15 drifting buoys used in the analysis.

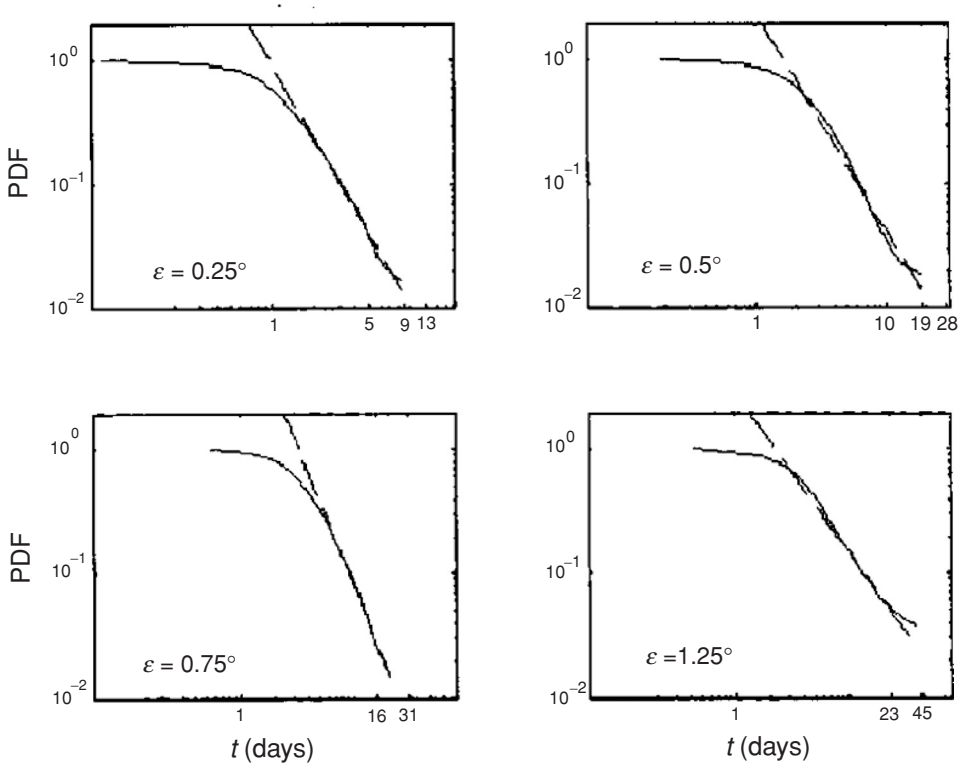

Figure 6.17 PDF of FPT (here labelled as PSP) calculated for different levels of tolerance ε. Solid and dashed lines are the PSP and the proposed theoretical power laws to approximate it for large times (from Ivanov and Chu 2007b).

P1: SJT Trim: 174mm × 247mm Top: 0.553in Gutter: 0.747in
CUUK726-06 cuuk726/Palmer ISBN: 978 0 521 76105 5 July 6, 2009 17:42

into the long FPT period (t larger than 1 day) demonstrates the existence of a long-term correlation between the drifter and synthetic particle trajectories. Such a phenomenon is called the extremely successful prediction (Chu *et al*. 2002a). This long tail has the power behaviour for a long FPT period with power exponents of 2.17, 1.98, 2.08 and 1.77 for ε values of 0.25°, 0.5°, 0.75° and 1.25°, respectively. For a power exponent larger than 2, there is no intermittency in the prediction skill.

Dependence of the first two FPT moments on the tolerance (ε) follows the power law

$$\langle \tau \rangle \sim \varepsilon^{0.99 \pm 0.08....}, \quad \hat{\tau}_2 \sim \varepsilon^{1.76 \pm 0.07.....}, \tag{6.44}$$

which indicates that the Lagrangian prediction skill of the Gulf of Mexico model is non-Gaussian and non-intermittent. If the FPT statistics is Gaussian, the power exponents of (6.44) should be

$$\alpha = 1, \quad \beta = 2,$$

rather than

$$\alpha = 0.99 \pm 0.08, \quad \beta = 1.76 \pm 0.07.$$

6.9 Conclusions

(1) First passage time (FPT) presents a new way to detect climate model predictability and temporal variability of the climate indices. It is a random variable, the probability density function of which satisfies the backward Fokker–Planck equation. In solving this equation, it is easy to obtain the ensemble mean and variance of the FPT for climate models and climate indices. The solution of the backward Fokker–Planck equation is usually non-Gaussian. The PDF of FPT for a numerical ocean model to uncertain initial conditions satisfies the three-parameter Weibull distribution.

(2) The FPTs for the five climate indices show Brownian fluctuations. This means that the early results on the Brownian fluctuations for the NAO index are also valid for the other indices (AO, AAO, PNA and SO). With $\delta \to 0$ as a limit case (i.e. no index reduction), the FPT density function tends to the δ function.

(3) The power law of FPT is found for climate model predictability. The probability density function of FPT for the Gulf of Mexico nowcast system is asymmetric with a broader and long tail for higher values which indicates long-term predictability. This long tail corresponds to the power law for error growth. For FPT with small mean and mode values, its individual model prediction can be valid for a long period (long-terms prediction); this is represented by a long tail for higher FPT values. The extreme long and short predictions share the same statistics.

P1: SJT Trim: 174mm × 247mm Top: 0.553in Gutter: 0.747in
CUUK726-06 cuuk726/Palmer ISBN: 978 0 521 76105 5 July 6, 2009 17:42

(4) The power law of FPT is also found in climate index prediction. For a very small values of the index reduction, ρ_0 (0.01 for the AO, AAO, NAO, and PNA indices and 0.1 for SOI), the cumulative FPT density function shows a power-law dependence on τ_ρ with an exponent of approximately $-1/2$. Another well-known method for checking power-law dependence is examination of the autocorrelation function. This also confirms that the climate indices have Brownian-type fluctuations.

(5) The FPT is found useful to analyse stochastic stability of numerical models. It is expected that FPT will be applied to many areas such as stochastic climate prediction and stochastic dynamical systems.

Acknowledgements

The author thanks the Banff International Research Station (BIRS) for hosting the Workshop on Stochastic Dynamical Systems and Climate Modeling and the organisers Jinqiao Duan, Boualem Khouider, Richard Kleeman and Adam Monahan. The author also thanks Tim Palmer and Paul Williams for their work in editing this book.

References

Auclair, F., Marsaleix, P. & De Mey, P. 2003 Space–time structure and dynamics of the forecast error in a coastal circulation model of the Gulf of Lions. *Dyn. Atmos. Ocean*, **36**, 309–346.

Ausloos, M. & Ivanova, K. 2001 Power-law correlations in the Southern-Oscillation-index fluctuations characterizing El Niño. *Phys. Rev. E*, **63**, 047201.

Boffetta, G., Giuliani, P., Paladin, G. & Vulpiani, A. 1998 An extension of the Lyapunov analysis for the predictability problem. *J. Atmos. Sci*., **55**(23) 3409–3416.

Brasseur, P., Blayo, E. & Verron, J. 1996 Predictability experiments in the North Atlantic Ocean: outcome of a quasi-geostrophic model with assimilation of TOPEX/POSEIDON altimeter data. *J. Geophys. Res*., **101**, 14161–14173.

Chu, P. C. 1999 Two kinds of predictability in the Lorenz System. *J. Atmos. Sci*., **56**, 1427–1432.

Chu, P. C. 2006 First-passage time for stability analysis of the Kaldor model. *Chaos, Solitons & Fractals*, **27**, 1355–1368.

Chu, P. C. 2008 First passage time analysis for climate indices. *J. Atmos. Oceanic Technol*., **25**, 258–270.

Chu, P. C., Fan, C. W. & Ehret, L. L. 1997 Determination of open boundary conditions with an optimization method. *J. Atmos. Oceanic Technol*., **14**, 723–734.

Chu, P. C., Ivanov, L. M. & Fan, C. W. 2002a Backward Fokker–Planck equation for determining model valid prediction period. *J. Geophys. Res*., **107**, C6, 10.1029/2001JC000879.

Chu, P. C., Ivanov, L. M., Margolina, T. M. & Melnichenko, O. V. 2002b On probabilistic stability of an atmospheric model to various amplitude perturbations. *J. Atmos. Sci*., **59**, 2860–2873.

Chu, P. C., Ivanov, L., Kantha, L., Melnichenko, O. & Poberezhny, Y. 2002c Power law decay in model predictability skill. *Geophys. Res. Lett*., **29**(15), 10.1029/2002GLO14891.

Chu, P. C., Ivanov, L. M., Kantha, L. H. *et al*. 2004 Lagrangian predictabilty of high-resolution regional ocean models. *Nonlinear Proc. Geophys*., **11**, 47–66.

Chu, P. C. & Ivanov, L. M. 2005 Statistical characteristics of irreversible predictability time in regional ocean models. *Nonlinear Proc. Geophys*., **12**, 1–10.

Collette, C. & Ausloos, M. 2004 Scaling analysis and evolution equation of the North Atlantic oscillation index fluctuations. *Int. J. Mod. Phys. C*, **15**, 1353–1366.

Dalcher, A. & Kalnay, E. 1987 Error growth and predictability in operational ECMWF forecasts. *Tellus*, **39A**, 474–491.

Ding, M. & Yang, W. 1995 Distribution of the first return time in fractional Brownian motion and its application to the study of on–off intermittency. *Phys. Rev. E*, **52**, 207–213.

Downing, D. J., Gardner, R. H. & Hoffman, F. O. 1985. An examination of response-surface methodologies for uncertainty analysis in assessment of models. *Technometrics*, **27**, 2, 151–163.

Drosdowsky, W. 1994 Analog (nonlinear) forecasts of the Southern Oscillation index time series. *Weather Forecast*., **9**, 78–84.

Dymnikov, V. P. & Filatov, A. N. 1997 *Mathematics of Climate Modeling*. Birkhauser Publishing Co.

Farrell, B. F. & Ioannou, P. J. 1996 Generalized stability theory. Part 1. Autonomous operations. *J. Atmos. Sci*., **53**, 14,2025–14,2040.

Gardiner, C. W. 1985 *Handbook of Stochastic Methods for Physics*, *Chemistry and the Natural Sciences*. Springer-Verlag.

Good, P. I. 1996 *Re-Sampling Methods. A Practical Guide to Data Analysis*. Birkhauser Publishing.

Ivanov, L. M., Kirwan, A. D. Jr. & Melnichenko, O. V. 1994 Prediction of the stochastic behavior of nonlinear systems by deterministic models as a classical time-passage probabilistic problem, *Nonlinear Proc. Geophys*., **1**, 224–233.

Ivanov, L. M. & Chu, P. C. 2007a On stochastic stability of regional ocean models to finite-amplitude perturbations of initial conditions. *Dyn. Atmos. Oceans*, **43** (3–4), 199–225.

Ivanov, L. M. & Chu, P. C. 2007b On stochastic stability of regional ocean models with uncertainty in wind forcing. *Nonlinear Proc. Geophys*., **14**, 655–670.

Kaneko, K. 1998 On the strength of attractors in a high-dimensional system. Milnor attractor: Milnor attractor network, robust global attraction, and noise-induced selection. *Physica* D, **124**, 322–344.

Keppenne, C. L. & Ghil, M. 1992 Adaptive spectral analysis and prediction of the Southern Oscillation index. *J. Geophys. Res*., **97**, 20449–20454.

Lacarra, J. F. & Talagrand, O. 1988 Short-range evolution of small perturbations in a barotropic model. *Tellus*, **40A**, 81–95.

Latin hypercube sampling tool, 2001: http://www.mathepicomepitoos/hs/nrpage.html.

Lind, P. G., Mora, A., Gallas, J. A. C. & Haase, M. 2005 Reducing stochasticity in the North Atlantic Oscillation index with coupled Langevin equations. *Phys. Rev. E*, **72**, 056706.

Lorenz, E. N. 1984 Irregularity. A fundamental property of the atmosphere. *Tellus*, **36A**, 98–110.

Maharaj, E. A. & Wheeler, M. J. 2005 Forecasting an index of the Madden–Julian Oscillation. *Int. J. Climatol*., **25**, 1611–1618.

P1: SJT Trim: 174mm × 247mm Top: 0.553in Gutter: 0.747in
CUUK726-06 cuuk726/Palmer ISBN: 978 0 521 76105 5 July 6, 2009 17:42

Mariano, A. J., Griffa, A., Ozgokmen, T. M. & Zambiancji, E. 2002 Lagrangian analysis and predictability of coastal and ocean dynamics 2000. *J. Atmos. Oceanic Technol*., **19**, 1114–1126.

Nicolis, C. 1992 Probabilistic aspects of error growth in atmospheric dynamics. *Q. J. R. Meteorol. Soc*., **118**, 553–568.

Palmer, T. N. 2001 A nonlinear dynamical perspective on model error: a proposal for non-local stochastic-dynamic parameterisation in weather and climate prediction models. *Q. J. R. Meteorol. Soc*., **127**, 279–304.

Rangarajan, G. & Ding, M. 2000 First passage time distribution for anomalous diffusion. *Phys. Lett. A*, **273**, 322–330.

Sabel'feld, K. 1991 *Monte-Carlo Methods in Boundary Value Problems*. Springer-Verlag.

Schneider, T. & Griffies, S. H. 1999 A conceptual framework for predictability studies. *J. Climate*, **12**, 3133–3155.

Sura, P., Fraedrich, K. & Lunkeit, F. 2001 Regime transitions in a stochastically forced double-gyre model. *J. Phys. Oceanogr*., **31**, 411–426.

Tikhonov, V. I. & Khimenko, V. I. 1998 Level-crossing problems for stochastic processes in physics and radio engineering: a survey. *J. Comput. Tech. Electr*., **43**, 457–477.

Torrence, C. & Campo, G. P. 1998 A practical guide to wavelet analysis. *Bull. Am. Meteor. Soc*., **79**, 62–78.

Toth, Z. & Kalnay, E. 1997 Ensemble forecasting at NCEP: the breeding method, *Mon. Weather Rev*., **125**, 3297–3318.

Toth, Z., Szunyogh, I., Bishop, C. *et al*. 2001 On the use of targeted observations in operational numerical weather predictions. Preprints, Fifth Symposium on Integrated Observing Systems, American Meteorological Society, January 15–19, Albaquerque, NM, pp. 72–79.

Veronis, G. 1966 Wind-driven ocean circulation, II: numerical solutions of the nonlinear problem. *Deep-Sea Res*., **13**, 31–55.

Vukicevic, T. 1991 Nonlinear and linear evolution of initial forecast errors. *Mon. Weather Rev*., **119**, 1602–1611.

Walker, G. T. & Bliss, E. W. 1937 World weather VI. *Mem. R. Meteorol. Soc*., **4**, 119–139.

White, H. 1994 *Estimation, Inference and Specification Analysis*. Cambridge University Press.

Wirth, A. & Ghil, M. 2000 Error evolution in the dynamics of an ocean general circulation model. *Dyn. Atmos. Ocean*, **32**, 419–431.

Wright, P. B. 1988 An atlas based on the COADS dataset: fields of mean wind, cloudiness and humidity at the surface of global ocean. Technical Report 14, Max-Plank-Institute fur Meteorology.